Geochemistry, Geophysics, Geosystems

RESEARCH ARTICLE
10.1029/2020GC009434

Key Points:

- Heterogeneous high stress deformation is observed in peridotites from the Eastern Southwest Indian ridge
- Stress and strain concentrations produce localized grain size reduction by dynamic recrystallization in olivine rich-domains
- This deformation likely occurs at the root of axial detachment faults in magma-starved mid-ocean ridges

Supporting Information:

Supporting Information may be found in the online version of this article.

Correspondence to:

M. Bickert,
manon.bickert@unimore.it

Citation:

Bickert, M., Cannat, M., Tommasi, A., Jammes, S., & Lavier, L. (2021). Strain localization in the root of detachment faults at a melt-starved mid-ocean ridge: A microstructural study of abyssal peridotites from the Southwest Indian Ridge. *Geochemistry, Geophysics, Geosystems*, *22*, e2020GC009434. https://doi.org/10.1029/2020GC009434

Received 15 SEP 2020
Accepted 19 MAR 2021

Strain Localization in the Root of Detachment Faults at a Melt-Starved Mid-Ocean Ridge: A Microstructural Study of Abyssal Peridotites From the Southwest Indian Ridge

M. Bickert[1,2], M. Cannat[1], A. Tommasi[3], S. Jammes[4], and L. Lavier[5]

[1]Marine Geosciences, Institut de Physique du Globe de Paris, UMR 7154 -CNRS, Université de Paris, Paris, France, [2]Now at Dipartimento di Scienze Chimiche e Geologiche, Università di Modena e Reggio Emilia, Modena, Italy, [3]Géosciences Montpellier, CNRS & Université de Montpellier, Montpellier, France, [4]Department of Geography, Texas State University, San Marcos, TX, USA, [5]Department of Geological Sciences, Jackson School of Geosciences, Institute for Geophysics, The University of Texas at Austin, Austin, TX, USA

Abstract Detachment faults that exhume mantle peridotites to the seafloor play a major role in the accommodation of plate divergence at slow-spreading ridges. Using 99 samples of partially serpentinized peridotites dredged from a nearly amagmatic segment of the eastern part of the Southwest Indian Ridge, we characterize the deformation processes active in the root zone of detachment fault systems. The deformation is heterogeneous even at the sample scale and combines both brittle and crystal-plastic mechanisms. Strain localization is initially controlled by strength contrasts at the grain scale between olivine and orthopyroxene and between variably oriented olivine crystals. Orthopyroxene deformation is primarily brittle (microfractures), but kink bands and dynamic recrystallization are locally observed. In contrast, olivine deforms primarily by dislocation creep with dynamic recrystallization under high deviatoric stresses (80–270 MPa). Olivine grains poorly oriented to deform by dislocation glide display kink bands and localized microfractures. Dynamic recrystallization controlled by strain and stress concentrations produce anastomosing zones of grain size reduction (GSR). GSR zones contain limited late to post-kinematic amphibole, suggesting the presence of small volumes of hydrous fluids. Plagioclase, when present, is post-kinematic. This heterogeneous high-stress deformation is observed, with variable intensity, in every sample investigated, suggesting that it was pervasively distributed in the root region of axial detachments. Abyssal peridotite samples from more magmatically robust slow mid-ocean ridges do not show this pervasive high stress deformation microstructure, implying magma, when present, tends to localize most of the strain at the root of axial detachment systems.

1. Introduction

Large-offset normal faults, which exhume mantle peridotites, play a significant role in plate divergence at slow-spreading ridges (Cann et al., 1997; Cannat, 1993; Cannat et al., 2006; Escartín et al., 2008; Sauter et al., 2013; Smith et al., 2006). These faults, also called detachment faults, have a concave-downward shape; they are thought to initiate at a steep dip and have their footwall rotated to shallow dipping angles with increased fault slip (de Martin et al., 2007; Garcés & Gee, 2007; MacLeod et al., 2002; Morris et al., 2009; Smith et al., 2006). They are assumed to root in the brittle-ductile transition (BDT). BDT depths at slow spreading ridges are estimated from maximum depths of axial microearthquakes: they are at least 10 km in detachment-dominated regions of the Mid-Atlantic Ridge (MAR) (de Martin et al., 2007; Parnell-Turner et al., 2018) and at least 15 km in magma-poor regions of the ultraslow Southwest Indian Ridge (SWIR) (Grevemeyer et al., 2019; Schlindwein & Schmid, 2016; Yu et al., 2018).

The development of oceanic detachment faults is controlled by the respective contributions of tectonism and magmatism to plate divergence (Behn & Ito, 2008; Buck et al., 2005). If melt supply is sufficient, less movement is needed along the faults to accommodate plate divergence. Numerical models that include melt emplaced as dikes in the brittle lithosphere suggest that ridge settings receiving sufficient melt to accommodate approximately half of the plate divergence are the most favorable for development of long-lived detachments (Buck et al., 2005; Tucholke et al., 2008). This scenario is likely the case at the slow spreading MAR, where detachments expose gabbroic and ultramafic rocks at the seafloor in their footwall (Cannat & Casey, 1995; Cannat et al., 1995; Dick et al., 2003), while basalts are emplaced in the hanging wall (MacLeod

et al., 2009). These long-lived detachments are thought to root into a BDT region weakened by regular melt injections (Cannat, 1991; Grimes et al., 2008; Ildefonse et al., 2007; Olive et al., 2010; Picazo et al., 2012). Geological observations attest to strong melt-rock interaction and to melt-assisted deformation along these detachment faults, including common localized deformation in gabbroic rocks and in peridotites adjacent to magmatic veins (Boschi et al., 2006; Cannat, 1991; Cannat & Casey, 1995; Ceuleneer & Cannat, 1997; Dick et al., 2002; Hansen et al., 2013; Picazo et al., 2012; Schroeder & John, 2004). Strain localization in melt-rich domains in the deep mantle sections of the MAR detachments is further supported by the observation that the bulk of the peridotites sampled outside transform fault domains retains the high-temperature, low-stress crystal-plastic deformation textures typical of lower lithosphere-asthenospheric flow (Achenbach et al., 2011; Ceuleneer & Cannat, 1997; Harigane et al., 2016; Seyler et al., 2007).

Tectonic processes are even more important in magma-starved mid-ocean ridges, but the active processes allowing for deformation at and below the BDT are less well constrained. The easternmost part of the SWIR, east of the Melville Fracture Zone, comprises regions where spreading occurs with very little magma input (Cannat et al., 2006; Sauter et al., 2013). Microseismicity studies in the region suggest a thick brittle lithosphere, at least 15 km (Chen et al., 2020) and possibly >20 km thick (Schlindwein & Schmid, 2016). Numerical models of oceanic spreading in melt-poor settings (Lavier & Buck, 2002; Tucholke et al., 2008) predict relatively short-lived normal faults with limited slip, instead of long-lived detachments. Yet geological observations from the SWIR record slip on detachment faults that regularly flip polarity, and last up to 1.5 Myr (Cannat et al., 2019; Reston, 2018; Sauter et al., 2013). These observations suggest that weakening mechanisms other than the presence of magma are at play in the deep lithosphere to allow protracted slip on such long-lived detachment faults (Bickert et al., 2020).

To document the deformation mechanisms at play in the root of a detachment fault in a melt-starved ridge segment, we analyze the microstructures of 99 moderately serpentinized samples dredged in the eastern SWIR. In a previous paper (Bickert et al., 2020), we targeted a subset of the most deformed samples, showing evidence for localized crystal-plastic to semi-brittle deformation at temperatures of 800–1,000°C and high stresses (estimated as 80–270 MPa based on recrystallized grain size piezometry). Here, we provide a detailed textural and microstructural analysis of the entire sample set, documenting the mechanisms of strain localization that may facilitate the development of detachment faults at melt-starved slow and ultraslow spreading ridges.

2. Sampling

Samples analyzed in this study have been dredged during the *Smoothseafloor* cruise (2010; R/V Marion Dufresne; Table S1) along two corridors of nearly amagmatic spreading in the eastern part of the SWIR, between 62°E and 65°E (Figure 1; Sauter et al., 2013). The SWIR in this region has an overall weak magma supply (Cannat et al., 1999; Minshull et al., 2006). Magma is focused along-axis to discrete volcanic centers, leaving corridors of nearly amagmatic spreading that expose variably serpentinized mantle-derived rocks (Figure 1; Sauter et al., 2013). Of the 33 dredges located in these nearly amagmatic corridors, 29 recovered variably serpentinized peridotites (Figure 1). These ultramafic rocks are interpreted as exhumed over the past 10 Myr by successive axial detachment faults with flipping polarity ("flip-flop"; Cannat et al., 2019; Sauter et al., 2013; Reston, 2018). Gabbroic rocks (magmatic crustal material) constitute only 2% of the dredged samples and basalts, 16% (Sauter et al., 2013). The position of the dredges with respect to the flip-flop detachment pattern proposed by Sauter et al. (2013) and Cannat et al. (2019) is shown in Figure 2.

Based on the examination of 385 thin sections, we determined: (1) the proportion of partially and extensively serpentinized peridotite samples, and (2) plagioclase-bearing peridotite samples in each dredge (Figure 2 and Table 1). Ninety-nine partially serpentinized samples, from 13 dredges, contain sufficient primary peridotite mineralogy (<70% serpentinization) for microstructural analysis (Table S2). Ten of these 13 dredges come from the western nearly amagmatic corridor and 3 from the eastern nearly amagmatic spreading corridor (Figure 1), with 7 dredges from the near-axis or axial regions. Twelve of the 13 dredges sample the footwall of successive flip-flop detachments formed in a nearly amagmatic context. These dredges contain on average 12% plagioclase-bearing serpentinized peridotites (Figure 2 and Table 1) and <4% gabbros (Figure 1; Sauter et al., 2013). DR33 (Figure 2b) is the only dredge that sampled a moderately magmatic,

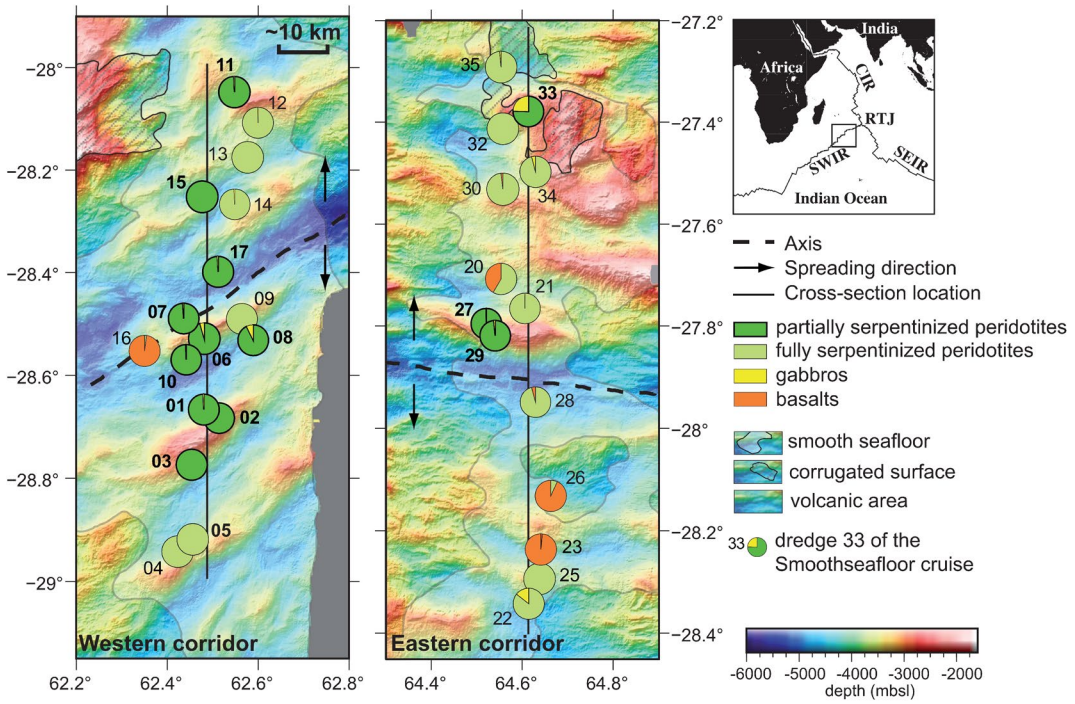

Figure 1. Bathymetric maps of the two nearly amagmatic spreading corridors sampled at and near the axis (black dashed line) of the eastern Southwest Indian Ridge in the 62–65°E region (modified from Rouméjon et al., 2015; after Sauter et al., 2013). Pie charts show proportions of dredge samples recovered by rock type. Dredges that recovered partially serpentinized peridotites are highlighted (dredges with only fully serpentinized peridotites are represented in paler green). North-South solid black lines indicate the location of the cross-sections in Figure 2; note that the western transect is oblique to the ridge axis.

corrugated, detachment footwall (Cannat et al., 2009). It contains 40% plagioclase-bearing serpentinized peridotites and 25% gabbros (Figure 1; Sauter et al., 2013).

3. Methods

3.1. Microscopy

Microstructures were analyzed in thin sections of the 99 selected samples, using both optical polarizing and scanning electron microscopy (SEM). Deformation features being 3D, we studied three orthogonal thin sections for 24 samples. When the foliation could be identified in the macroscopic specimen, two mutually orthogonal sections were cut perpendicular to foliation. Deformation was characterized based on olivine and pyroxene grain size and shape, the presence of undulose extinction, subgrain boundaries, recrystallized grains, kink bands in both minerals and the distribution and geometry of grain size reduction (GSR) zones. SEM Electron backscattered images were used to characterize mineral assemblages in GSR zones. For 19 selected thin sections from 14 samples we drew microstructural sketches based on high-resolution micrographs (Figures 4–7). We also examined thin sections from the 286 more extensively serpentinized samples, looking for evidence of kink bands, recrystallization, and GSR zones in the primary assemblage (Table 1).

3.2. Electron Backscattered Diffraction (EBSD)

The crystallographic preferred orientation (CPO) of olivine, pyroxenes, spinel, and amphibole was measured in 17 selected samples using a JEOL JSM 5600 at the Geosciences Montpellier EBSD facility, with 17 kV acceleration voltage and 24 mm working distance. For each thin section, CPO maps covered areas of 4–13 cm^2 with a grid step of 15 or 35 μm, depending on olivine minimum grain size. Because of the large size of olivine porphyroclasts in most samples, CPO was measured on several thin sections and combined.

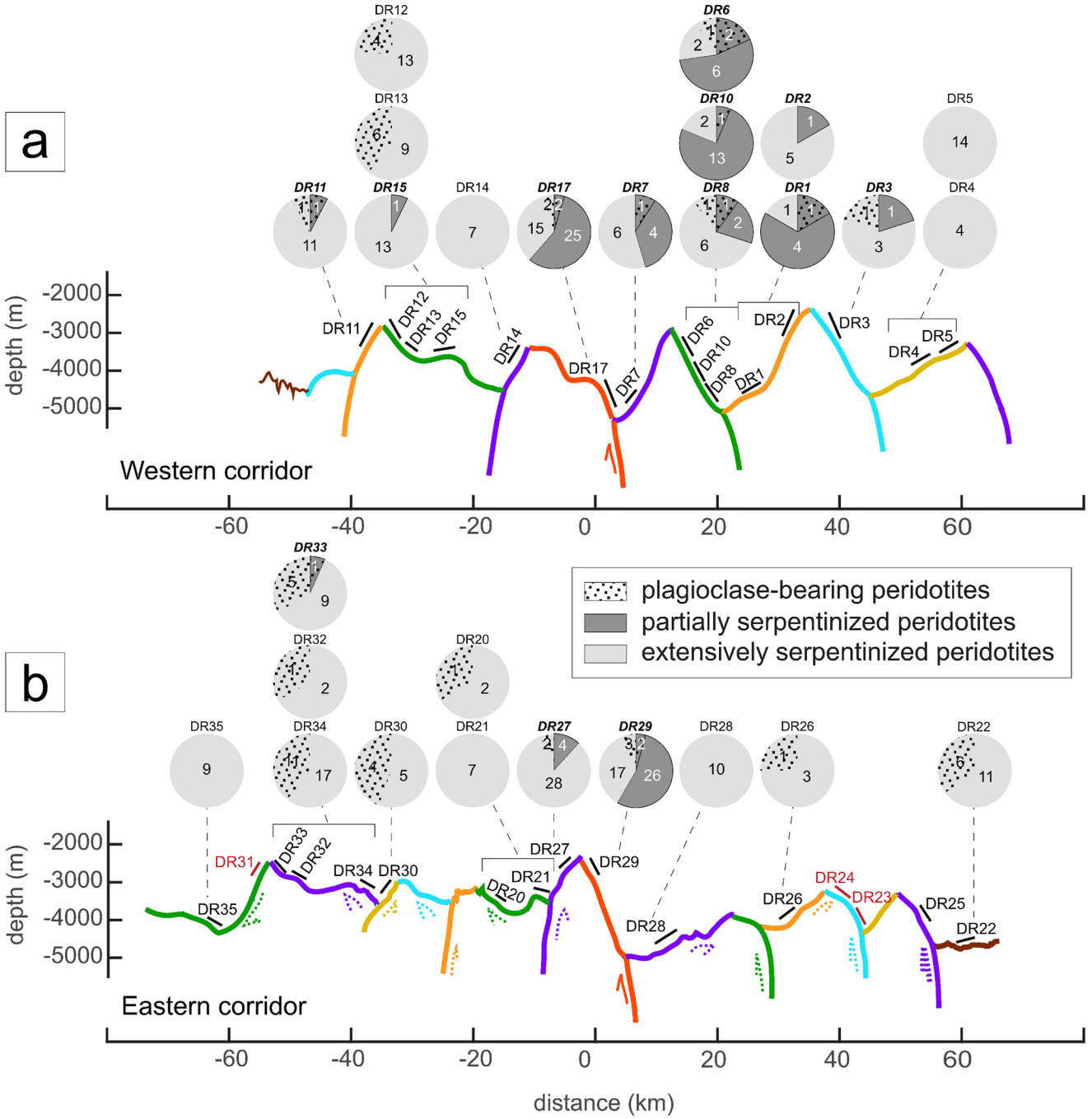

Figure 2. Cross-sections along the two nearly amagmatic spreading corridors shown in Figure 1: (a) Western corridor and (b) Eastern corridor. Cross-sections are adapted from Cannat et al. (2019), including the color code. Pie charts present the proportions of extensively or partially serpentinized peridotites, plagioclase-bearing or absent, in each dredge (dredges that recovered no serpentinized peridotites are numbered in red – DR23, DR24, DR31). Numbers in the pie charts are the number of samples for each lithology. Dredge locations (see Figure 1) are simplified so as to be represented along a single across-axis profile.

High-resolution CPO maps (grid step 0.5–10 μm depending on the dominant grain size) of fine-grained zones were also obtained for seven samples using the CamScan Crystal Probe X500-FEG SEM, also at the Geosciences Montpellier EBSD facility. Post-acquisition treatment consisted in deleting wild spikes and filling non- indexed pixels with ≥6 neighbors with coherent orientations with their average orientation.

CPO data were processed using the MTEX MATLAB toolbox (http://mtex-toolbox.github.io/; Bachmann et al., 2010; 2011). The orientation distribution functions (ODF) were calculated using a "de la Vallée

Geochemistry, Geophysics, Geosystems

10.1029/2020GC009434

Table 1

Deformation Features Identified in a Set of 385 Ultramafic Samples Selected in 29 Dredges (Smoothseafloor Cruise of RV Pourquoi Pas?; Sauter et al., 2013) in the 62°–65°E Region of the SWIR

Dredge	Number of ultramafic samples		Number of partially serpentinized samples		Deformation textures in variably serpentinized ultramafic samples						Deformation textures in partially serpentinized samples									
					Kinks in OPX		Recryst. px		GSR zones		Recryst. ol		A0		A1		A2		A3	
SMS-DR1	6	(1)	5	(1)	6	(1)	6	(1)	0	-	0	-	5	(1)	-	-	-	-	-	-
SMS-DR2	6	-	1	-	5	-	1	-	3	-	0	-	1	-	-	-	-	-	-	-
SMS-DR3	5	(1)	1	-	4	(1)	2	(1)	0	-	1	-	-	-	1	-	-	-	-	-
SMS-DR4	4	-	0	-	4	-	0	-	4	-	0	-	-	-	-	-	-	-	-	-
SMS-DR5	14	-	0	-	7	-	7	-	4	-	0	-	-	-	-	-	-	-	-	-
SMS-DR6	11	(3)	8	(2)	11	(3)	5	(3)	3	(1)	3	-	3	-	3	(1)	2	(1)	-	-
SMS-DR7	11	(1)	5	(1)	11	(1)	1	-	2	-	1	-	3	(1)	1	-	1	-	-	-
SMS-DR8	10	(2)	3	(1)	7	(2)	3	(1)	5	(1)	1	-	1	-	-	-	2	(1)	-	-
SMS-DR9	1	-	0	-	1	-	1	-	0	-	0	-	-	-	-	-	-	-	-	-
SMS-DR10	16	(1)	14	(1)	16	(1)	16	(1)	16	(1)	12	-	-	-	-	-	2	-	12	(1)
SMS-DR11	13	(2)	1	(1)	9	(2)	2	-	2	-	0	-	1	(1)	-	-	-	-	-	-
SMS-DR12	17	(4)	0	-	11	(3)	6	(1)	1	-	0	-	-	-	-	-	-	-	-	-
SMS-DR13	15	(6)	0	-	13	(5)	7	(5)	5	-	0	-	-	-	-	-	-	-	-	-
SMS-DR14	7	-	0	-	3	-	1	-	3	-	0	-	-	-	-	-	-	-	-	-
SMS-DR15	14	-	1	-	6	-	3	-	1	-	1	-	-	-	1	-	-	-	-	-
SMS-DR16	4	-	0	-	2	-	0	-	0	-	0	-	-	-	-	-	-	-	-	-
SMS-DR17	44	(4)	27	(2)	31	(3)	12	(1)	13	(2)	6	(1)	15	(1)	4	(1)	4	-	4	-
SMS-DR20	3	(1)	0	-	1	(1)	0	-	0	-	0	-	-	-	-	-	-	-	-	-
SMS-DR21	7	-	0	-	7	-	0	-	0	-	0	-	-	-	-	-	-	-	-	-
SMS-DR22	17	(6)	0	-	16	(6)	0	-	3	(1)	0	-	-	-	-	-	-	-	-	-
SMS-DR26	4	(1)	0	-	4	(1)	1	-	0	-	0	-	-	-	-	-	-	-	-	-
SMS-DR27	34	(2)	4	-	28	(2)	5	(1)	8	(1)	0	-	2	-	-	-	2	-	-	-
SMS-DR28	10	-	0	-	6	-	1	-	1	-	0	-	-	-	-	-	-	-	-	-
SMS-DR29	48	(5)	28	(2)	39	(4)	24	(4)	26	(1)	23	(1)	4	-	6	(1)	18	(1)	-	-
SMS-DR30	9	(4)	0	-	6	(4)	2	(2)	2	(1)	0	-	-	-	-	-	-	-	-	-
SMS-DR32	3	(1)	0	-	2	-	0	-	0	-	0	-	-	-	-	-	-	-	-	-
SMS-DR33	15	(6)	1	(1)	13	(4)	9	(4)	7	(3)	0	-	-	-	-	-	-	-	1	(1)
SMS-DR34	28	(11)	0	-	19	(9)	11	(6)	4	-	0	-	-	-	-	-	-	-	-	-
SMS-DR35	9	-	0	-	9	-	7	-	8	-	0	-	-	-	-	-	-	-	-	-
TOTAL	385	(62)	99	(12)	297	(53)	133	(31)	121	(12)	48	(2)	35	(4)	16	(3)	31	(3)	17	(2)
Proportion (partially serpentinized)	-	-	0.26	(0.12)	0.93	(0.92)	0.57	(0.75)	0.52	(0.42)	0.48	(0.17)	0.35	(0.33)	0.16	(0.25)	0.31	(0.25)	0.17	(0.17)

Table 1
Continued

Dredge	Number of ultramafic samples	Number of partially serpentinized samples	Deformation textures in variably serpentinized ultramafic samples						Deformation textures in partially serpentinized samples					
			Kinks in OPX		Recryst. px		GSR zones		Recryst. ol	A0	A1	A2	A3	
Proportion (extensively serpentinized)	-	-	0.74	(0.13)	0.72	(0.84)	0.27	(0.44)	0.24	(0.14)	-	-	-	-	-	-

In each dredge, we list: the number of serpentinized peridotite samples; the number of partially serpentinized samples; the number of variably serpentinized samples (both extensively and partially) that display key deformation features such as kink bands in orthopyroxene (OPX), recrystallized pyroxene (px), grain size reduction (GSR) zones; recrystallized olivine (ol) in partially serpentinized samples; and the number of partially serpentinized, olivine-bearing samples that display the following deformation textures: A0 (protogranular), A1 (porphyroclastic with no GSR zones), A2 (porphyroclastic with discontinuous GSR zones), and A3 (foliated with continuous GSR zones). For each column in the table, the number of plagioclase-bearing samples is shown in brackets.

Poussin" kernel function with a half-width of 15°. CPO is presented as one crystallographic orientation per pixel in pole figures (lower hemispheric stereographic projections). To analyze quantitatively the microstructure, we used the grain recognition routine in MTEX (Bachmann et al., 2011) with a misorientation threshold of 15° between two neighboring pixels for defining grain boundaries. Subgrain boundaries were identified by misorientations between neighboring pixels of 2–15°. Intragranular deformation was characterized by analysis of the Kernel Average Misorientation (KAM) and Misorientation relative to the Mean Orientation of the grain (Mis-2Mean) maps. We were not able to correctly define the shapes of the coarser grains using this approach, since they are dissected by numerous serpentine-filled fractures. In contrast, small grains are well defined and their grain size and shape distributions were quantified using MTEX. Average grain sizes were used to estimate paleostresses based on the paleopiezometric relation of Van der Wal et al. (1993).

4. Microstructures and Mineralogy of the Partially Serpentinized Peridotites

Protolith compositions for the 99 selected samples include harzburgites, some of them clinopyroxene-rich, and lherzolites, with rare dunites (4%). Most samples contain coarse olivine and orthopyroxene grains (up to 2 cm in size, Figure 3a). Some peridotites contain domains enriched in ortho- or clinopyroxene, forming a poorly defined compositional banding (Figures 3b and 3c). Plagioclase, now altered, was present as sparse impregnations (Figure 3b) in a few samples of most dredges (Figure 2). In hand specimen, most samples show no (Figure 3a) or a weak shape preferred orientation of the primary minerals (Figure 3c). A few samples show a foliation marked by elongated patches of pyroxene and by oriented GSR zones in olivine-rich domains (Figure 3d). Later serpentine and carbonate veins crosscut these microstructures (Figure 3d).

In thin section, all 99 "fresh" samples show some degree of spatially heterogeneous deformation of the primary mineralogy in the form of kink bands in orthopyroxene (93% of the samples; Table 1), fine-grained olivine and pyroxene resulting from recrystallization (48% and 57% of the samples, respectively), or GSR zones (GSR, 52% of the samples). GSR zones are defined in this study as planar or lens-shaped domains composed of fine-grained aggregates of olivine or olivine + orthopyroxene ± clinopyroxene + spinel ± amphibole, depending if formed within olivine grains or in contact with pyroxenes (Figure 3d). Grain sizes in the GSR zones range from 1.5 to 84 μm (Bickert et al., 2020), whereas the adjacent porphyroclasts are up to 2 cm long. The marked difference in grain size defines sharp-cut limits for the GSR (Figure 3d). GSR zones often have finite lengths, being a few mm to a few cm long, but in the most deformed samples, they form anastomosing networks crosscutting the entire sample (Figure 3d). Similar microstructures have been described in peridotites from a transform fault in the New Caledonia ophiolite by Chatzaras et al. (2020), who named them microdeformation zones (MDZs). Here, we favor the nomenclature of GSR zones because it highlights the main characteristics of these zones and carries no pre-judgment on the processes producing them. In the 286 more extensively serpentinized samples, the proportion of samples displaying these deformation features is lower (Table 1), likely due to serpentinization overprint.

We defined four textural types based on the occurrence of the deformation features listed in Table 1: from the least (A0) to the most deformed (A3). Textural type A0 (35% of the 99 partially serpentinized samples; Table 1) has kinked pyroxenes, but neither kinked nor recrystallized olivine nor GSR zones (Figure 4a). Textural type A1 (16% of the partially serpentinized samples) has kinked pyroxenes, rare kink bands in olivines (Figures 4b and 4c), and minor recrystallization of both olivine and pyroxene (Figures 4d and 4e), but no GSR zones. Textural type A2 (31% of the partially serpentinized samples) has kinked pyroxenes; both olivine and pyroxene recrystallize forming thin and discontinuous GSR zones (Figures 5 and 6). Finally, textural type A3 (17% of the partially serpentinized samples) has kinked pyroxenes and GSR zones that can be observed throughout the thin section (Figure 7a) and in the hand specimen (Figure 3d).

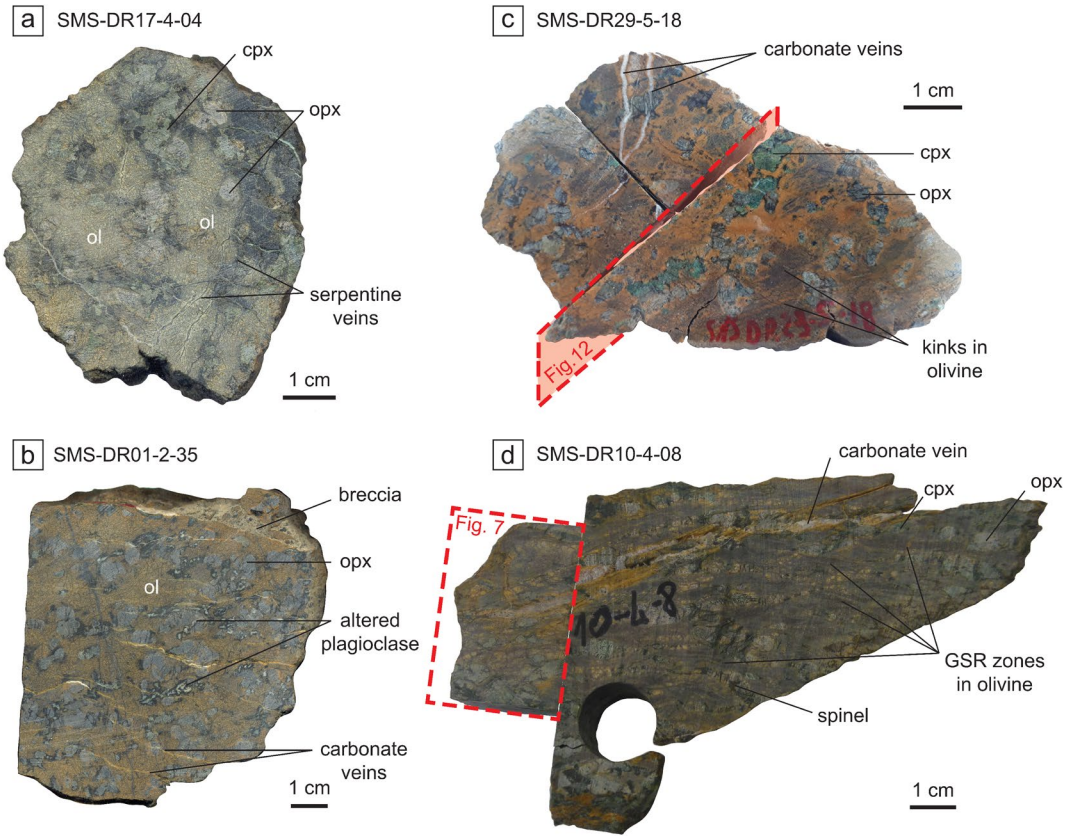

Figure 3. Photographs of partially serpentinized ultramafic rocks dredged along the two amagmatic corridors shown in Figure 1. Dashed red lines outline the location of thin sections displayed in Figures 7 and 12. (a) Weakly deformed partially serpentinized harzburgite (sample SMS-DR17-4-04) containing coarse orthopyroxene (opx), clinopyroxene (cpx), and olivine relicts (ol) in a partially serpentinized mesh textured matrix. (b) Partially serpentinized plagioclase-bearing harzburgite (SMS-DR01-2-35). Texture is similar to (a) but mesh-textured serpentinized olivine domains are oxidized and sample contains veins of carbonate and carbonated breccia. Plagioclase is altered and occurs as irregular interstitial patches, mostly associated with orthopyroxene. (c) Deformed partially serpentinized lherzolite (sample SMS-DR29-5-18). Texture is weakly foliated, the mesh-textured serpentinized olivine domains are oxidized and sample contains carbonate veins. Faint linear features in mesh-textured domain at the bottom of the picture correspond to prominent kink bands in the original olivine (see Figure 12). (d) Strongly deformed partially serpentinized lherzolite (sample SMS-DR10-4-08). Texture is strongly foliated with elongated pyroxene porphyroclasts and anastomosed grain size reduction (GSR) zones.

Plagioclase occurs in 12% of the 99 samples studied (and in 16% of the entire suite of 385 samples, including those showing extensive serpentinization; Table 1). This proportion is similar in all textural types (Table 1). Plagioclase occurs as interstitial grains in the primary assemblage, locally forming rims around spinel grains. It also occasionally forms plagioclase-rich veins, up to a few mm-thick (Figure S1). In each case, textures indicate that plagioclase crystallized after the deformation of the other primary minerals (Figure S1; Paquet et al., 2016).

A few samples contain <2% amphibole, which occurs mostly as prismatic or fibrous crystals in postkinematic veins, and occasionally as polygonal or prismatic grains in the GSR zones. Amphiboles in GSR zones are mostly Mg-rich hornblendes, whereas those in the veins are tremolites. Representative microprobe analyses of these amphiboles are available in Table S3. Major element compositions of pyroxenes and spinel in selected samples are accessible in the supplementary material of Bickert et al. (2020).

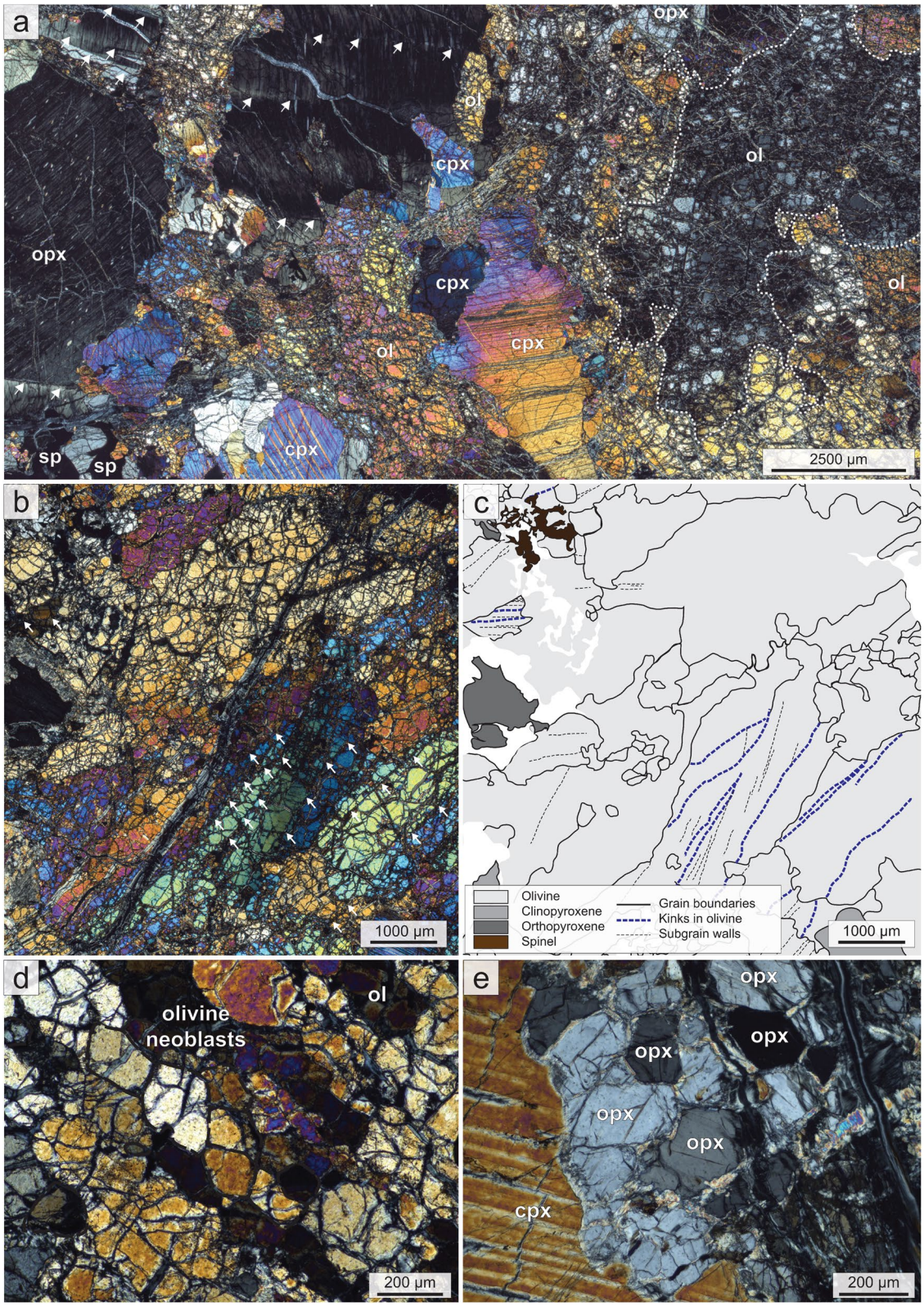
a
opx
ol
cpx
ol
opx
cpx
ol
cpx
ol
cpx
sp
sp
cpx
2500 µm
b
1000 µm
c
Olivine
Clinopyroxene
Orthopyroxene
Spinel
Grain boundaries
Kinks in olivine
Subgrain walls
1000 µm
d
olivine
neoblasts
ol
200 µm
e
opx
opx
opx
opx
opx
cpx
200 µm

4.1. Textural Type A0

The least deformed samples (Texture A0 in Table 1) preserve the texture of the peridotite protolith. Olivine and orthopyroxene occur as irregularly shaped grains ranging from a few millimeters to several centimeters (Figure 4a). Olivine commonly has cuspate boundaries with orthopyroxene, a texture that has been interpreted as evidence for incongruent melting (Dick et al., 2002; Seyler et al., 2007). Clinopyroxene grains range from a few micrometers to several millimeters in size, and are often associated with orthopyroxene grains. Both pyroxenes commonly contain exsolution lamellae. Spinel grains have holly leaf to euhedral shapes and are either disseminated in the olivine matrix or associated with pyroxenes, forming clusters that might result from the breakdown of garnet (Brunelli et al., 2014; Seyler et al., 2003) or from partial crystallization of interstitial melts (Le Roux et al., 2008).

Coarse olivine grains show weak undulose extinction (Figure 4a) and occasional, widely spaced parallel subgrain boundaries. Orthopyroxene porphyroclasts are kinked (Figure 4a). They are locally associated with finer-grained aggregates composed of polygonal orthopyroxene and clinopyroxene neoblasts ranging between 100 and 300 μm, and interstitial spinel. Clinopyroxene also shows kinks, undulose extinction, and local recrystallization. The coexistence of kinked orthopyroxene with seemingly less deformed large olivine grains (Figure 4a) is intriguing; it suggests that some of the kinking may have occurred prior to the growth of the olivines, which would be coherent with observation of kinked orthopyroxenes in almost all samples, regardless of the olivine deformation features (Table 1).

4.2. Textural Type A1

Peridotites with textural type A1 (Figures 4b and 4c) host coarse, kinked pyroxene grains, locally rimmed by finer grained ortho- and clinopyroxene neoblasts similar to those observed in samples with textural type A0 (Figure 4e). However, in contrast to samples with texture A0, these peridotites show a more pronounced intracrystalline deformation of olivine, recorded as undulose extinction and subgrain boundaries, locally lined with coarse (80–100 μm) recrystallized grains (Figure 4d), and rare kink bands. The kink bands produce sharp variations in the grain orientation (marked by sharp contrast in polarization color); they are often lens-shaped and oblique to the undulose extinction and subgrain boundaries, the latter change orientation across the kink band (Figures 4b and 4c).

4.3. Textural Type A2

Textural type A2 is heterogeneous at thin section scale (Figures 5a and 5b) and does not result in a visible foliation at hand specimen scale (Figure 3c). Olivine porphyroclasts display frequent kink bands, marked undulose extinction, and, locally, tightly spaced subgrain boundaries (Figures 5a, 5b, 6a, and 6b). Orthopyroxene porphyroclasts are kinked and show undulose extinction (Figures 5a–5c). These peridotites show discontinuous GSR zones, dominantly located in olivine that is in contact with orthopyroxene porphyroclasts (Figures 5b–5e, 6b, and 6c). GSR zones also develop along kinks and microfractures in olivine porphyroclasts, forming a discontinuous anastomosed network (Figures 5e, 5f, 6c, and 6d). The spacing between subgrain boundaries and kink bands in olivine tends to decrease and kink bands tend to curve in the vicinity of GSR zones (Figures 5e and 6c). Microfractures tend to follow kink bands and subgrain boundaries within olivine grains (Figures 5c, 5e, 6b, and 6c). Locally, they are connected to the kink bands (Figures 5e, 6b, and 6c). GSR zones within olivine-rich domains are composed of very small olivine neoblasts (<50 μm; Figures 5f and 6d). GSR zones next to orthopyroxene porphyroclasts are polymineralic, with orthopyroxene, olivine, spinel, locally clinopyroxene and, in a few samples, minute amounts of polygonal or prismatic amphibole crystals (Figures 5d and 8a).

Figure 4. Textural types A0 and A1: Microphotographs (crossed-nicols) and sketch showing weakly to moderately deformed partially serpentinized peridotites. (a) Sample SMS-DR01-2-01. Texture A0 is characterized by centimeter-sized olivine (ol) and orthopyroxene (opx) with irregular shapes and cuspate boundaries (check the olivine grain outlined by the white dashed line), kink bands in orthopyroxene (white arrows), and undulose extinction with no visible subgrain boundaries in olivine and clinopyroxene. (b) Sample SMS-DR03-2-17. Texture A1 displays local subgrain boundaries and occasional kink bands in olivine (white arrows). (c) Sketch of deformation texture A1. Cracks and veins associated with serpentinization are not shown. (d) and (e) are details of sample SMS-DR03-2-17, showing (d): locally recrystallized grains of olivine, 80–100 μm in size; and (e): locally recrystallized orthopyroxene (opx), 100–300 μm in size.

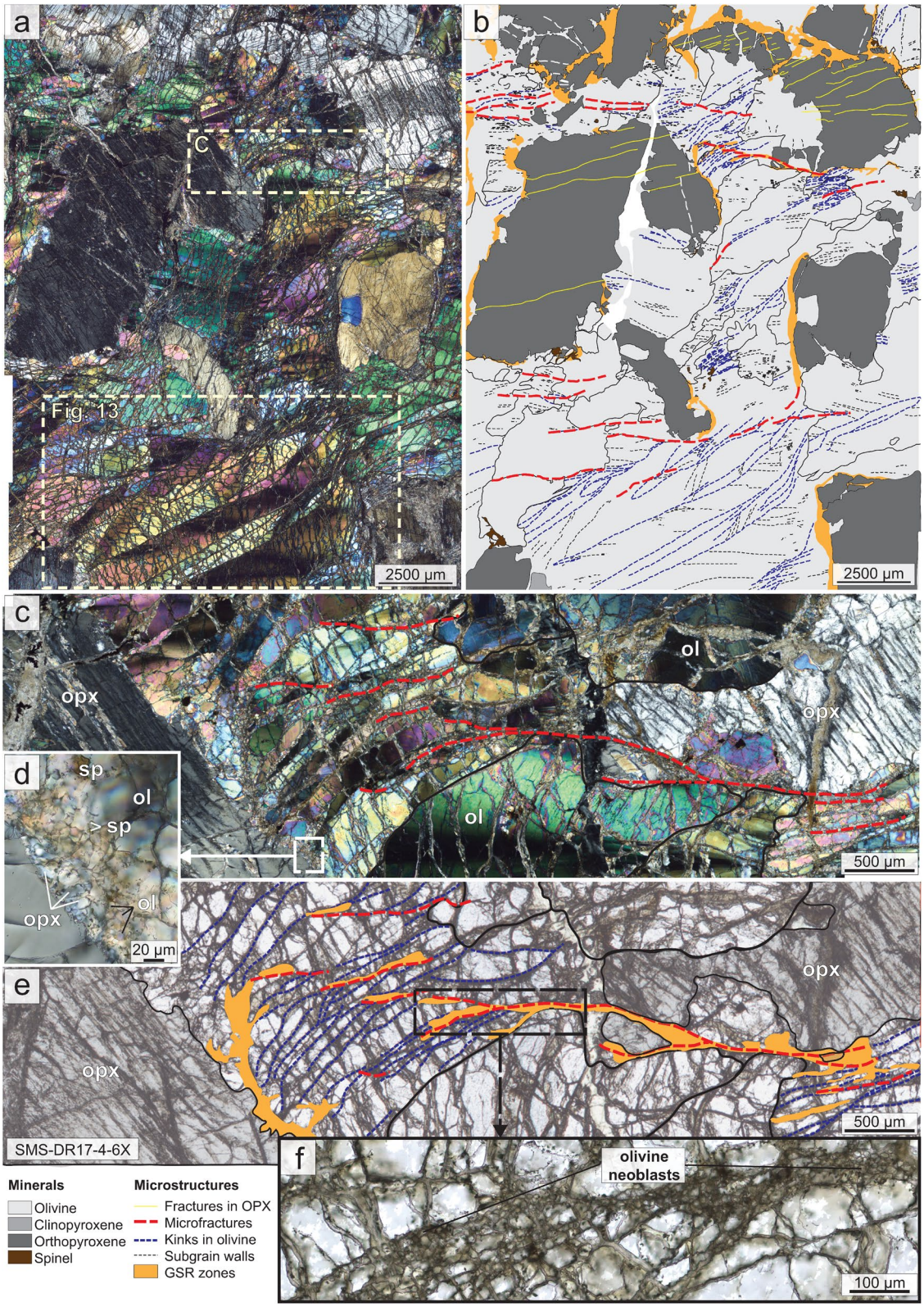
a
C
Fig. 13
2500 µm
b
2500 µm
c
opx
ol
opx
ol
500 µm
d
sp
ol
> sp
opx
ol
20 µm
e
opx
opx
500 µm
SMS-DR17-4-6X
f
olivine neoblasts
100 µm
Minerals
Olivine
Clinopyroxene
Orthopyroxene
Spinel
Microstructures
Fractures in OPX
Microfractures
Kinks in olivine
Subgrain walls
GSR zones

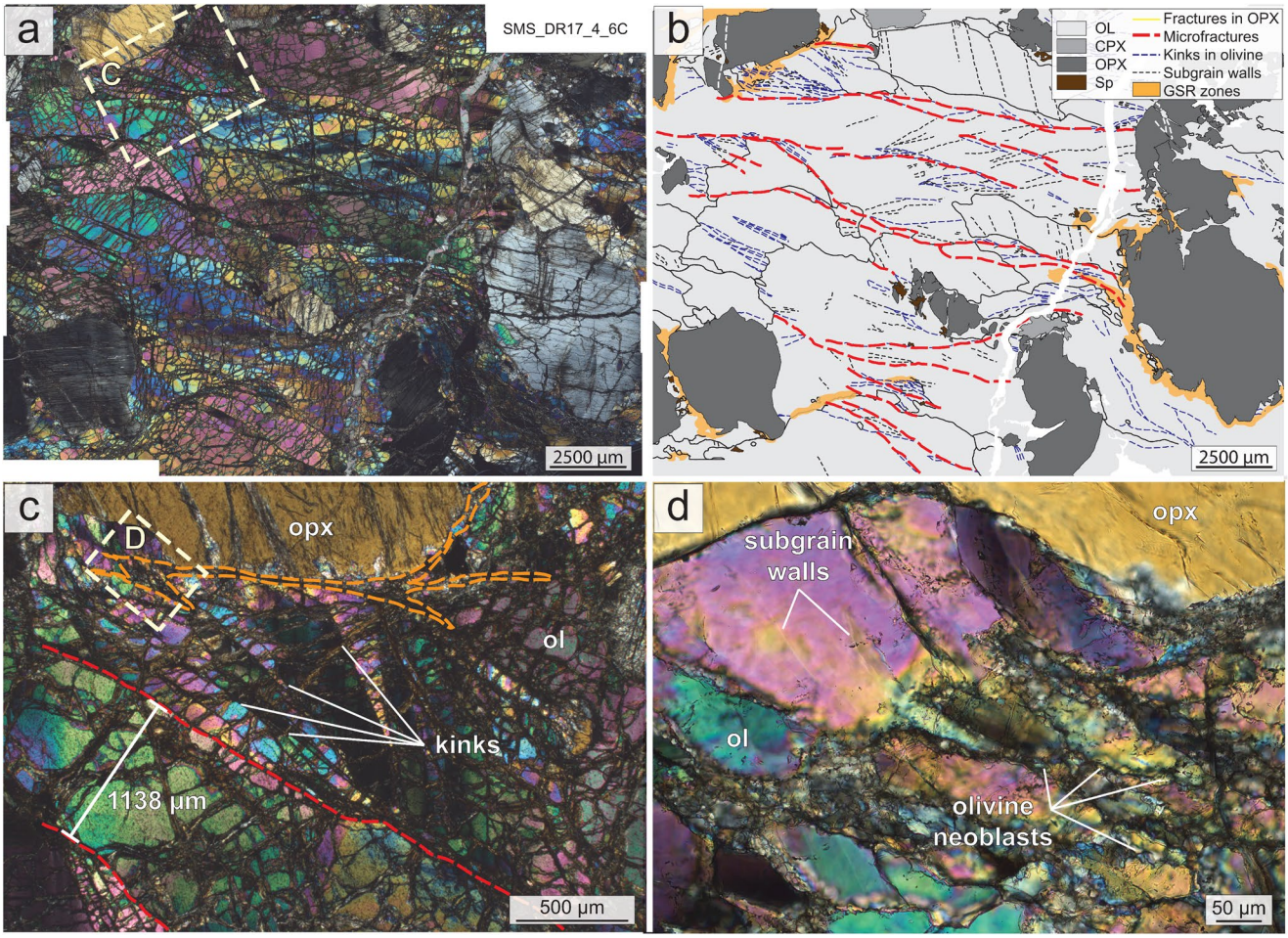

Figure 6. Microphotographs and associated sketch of kink bands, GSR zones and microfractures in olivine in textural type A2 samples. Sample SMS-DR17-4-6, thin section C, orthogonal to the thin section shown in Figure 5. (a) Crossed-nicols microphotograph and (b) structural interpretation (cracks and veins associated with serpentinization are not shown). Olivine is strongly deformed with kink bands, some of which are paralleled by microfractures. Kinked olivine displays marked undulose extinction and subgrain boundaries oblique to the kink bands. Kink bands in olivine share a preferred orientation at the thin section and sample scales. Microfractures follow olivine grain and subgrain boundaries. They branch into GSR zones next to orthopyroxene porphyroclasts. (c) Crossed-nicols microphotograph located in (a). Kink bands, some of which are paralleled by microfractures, form a horse-tail structure that branches into a larger microfracture (in red). A thin GSR zone (underlined by orange dashed line) develops next to the orthopyroxene porphyroclast. (d) Detail of (c). In the GSR zone, thin anastomosing domains of finely recrystallized olivine grains develop along the kink bands.

4.4. Textural Type A3

Textural type A3 is characterized by GSR zones that crosscut an entire thin section (Figure 7a). They define a macroscopic foliation at hand specimen scale (Figure 3d). Type A3 peridotites have a heterogeneous microstructure at thin section scale; domains away from the main GSR zones have type A2 microstructural characteristics (Figures 7b, 7c, and 8b). GSR zones are a few micrometers to a few millimeters thick (Figures 7d, 7e, and 8c). The thicker GSR zones develop in olivine-rich domains (Figure 7d). They form

Figure 5. Textural type A2: Microphotographs and associated sketches showing heterogeneously deformed and partially serpentinized peridotites. Sample SMS-DR17-4-6. (a) Crossed-nicols microphotograph and (b) associated structural interpretation (cracks and veins associated with serpentinization are not shown). Olivine is strongly deformed with kink bands (blue dashed lines), some of which are paralleled by microfractures; kinked olivine domains display marked undulose extinction and subgrain boundaries oblique to the kink bands. Kink bands in olivine share a preferred orientation at the thin section and sample scales. Most grain size reduction (GSR) zones are located in olivine-rich domains near orthopyroxene porphyroclasts (b). Microfractures (red dashed lines in b, c, and e) follow olivine grain and subgrain boundaries, and olivine GSR zones. (c–f) Details of deformation features under polarized (c) and natural light (e), overlain by the structural interpretation. Kinking and microfracturing in olivine form interconnected structures and are more intense in the vicinity of GSR zones. (d) GSR zones along orthopyroxene porphyroclasts are composed by a polymineralic fine-grained assemblage of olivine, orthopyroxene, spinel, and occasional clinopyroxene (not shown). (f) Within olivine crystals, GSR zones are composed by very small olivine neoblasts (Table S4).

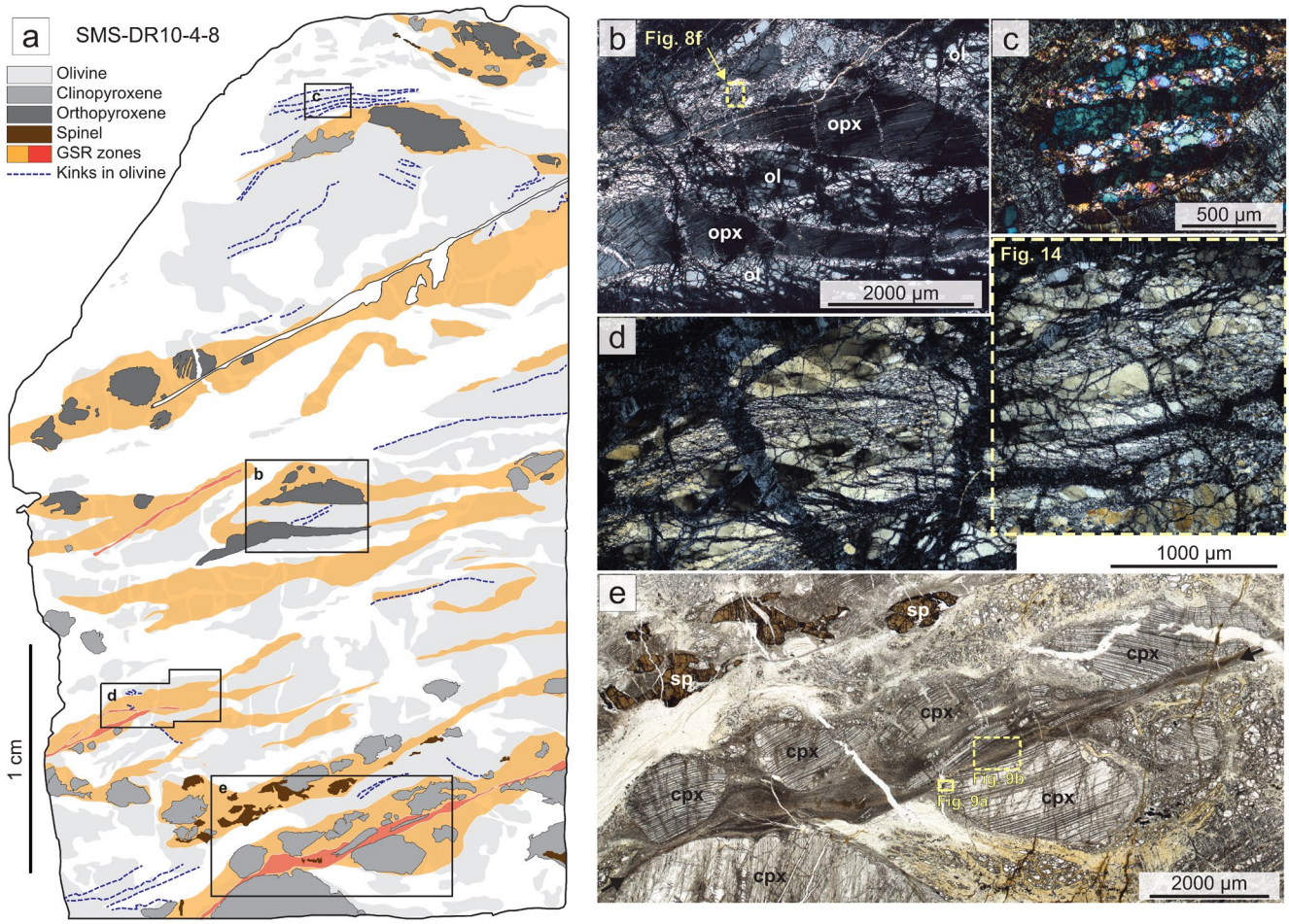

Figure 7. Textural type A3: Sketch and microphotographs showing extensively deformed, foliated, and partially serpentinized peridotites. Sample SMS-DR10-4-8. (a) Structural interpretation (cracks and veins associated with serpentinization and later alteration are not shown). The thin section is cut perpendicular to the GSR zones but we were not able to determine the lineation. (b–d) Crossed-nicols microphotographs are located in (a). (a) The sample is characterized by an alternation of olivine-rich and pyroxene rich-layers. GSR zones (in orange) have a strong preferred orientation and underline a foliation that is visible at the sample scale (Figure 3d). Dark and extensively altered microshear zones (darker orange) and amphibole veins (white) locally overprint the GSR zones, with the same geometry. (b) Orthopyroxene grains (opx) rounded to ribbon-like shapes. (c) The upper part of the thin section is less intensely foliated: olivines display kink bands with subgrain boundaries and partial recrystallization in relatively coarse polygonal aggregates along kink bands. (d) Olivine-rich domain with anastomosing GSR zones enclosing kinked porphyroclasts. (e) GSR zones in a spinel-rich (top) and a pyroxene-rich domains (bottom). Both spinel (sp) and clinopyroxene (cpx) porphyroclasts have sigmoidal tails of recrystallized neoblasts aligned in the foliation. The clinopyroxene-rich GSR zone is cut by a later shear zone indicated by black arrows (darker orange in (a)) that contains an extensively altered assemblage of olivine, clinopyroxene and spinel neoblasts.

anastomosing networks that crosscut the olivine porphyroclasts (Figures 7a and 7d). Neoblasts of olivine in these GSR zones vary from 1.5 to 84 µm in size; the sizes of the neoblasts are heterogeneous at sample scale, and between different domains of a single GSR zone (Bickert et al., 2020). Orthopyroxene grains within GSR zones may be elongated and are often fractured, but rounded crystals are also observed (Figures 7a and 7b). As in the textural types A0 to A2, orthopyroxene shows undulose extinction and kink bands.

Recrystallized assemblages differ between GSR zones formed in olivine-rich domains and along orthopyroxene porphyroclasts. The latter comprise a mixture of olivine and pyroxenes with irregular, interpenetrating phase boundaries and small interstitial spinel (Figures 8b, 8d–8f). In some GSR zones (Figures 8b and 8d), orthopyroxene grains appear as relicts of porphyroclasts rather than neoblasts; clinopyroxene and olivine have interstitial shapes. In other polymineralic GSR zones, however, orthopyroxene has interstitial or rounded shapes (Figures 8e and 8f). Well-developed GSR zones also affect clusters of clinopyroxene and/or spinel grains (Figure 7e). In these cases, clinopyroxene and spinel are deformed plastically and recrystallize,

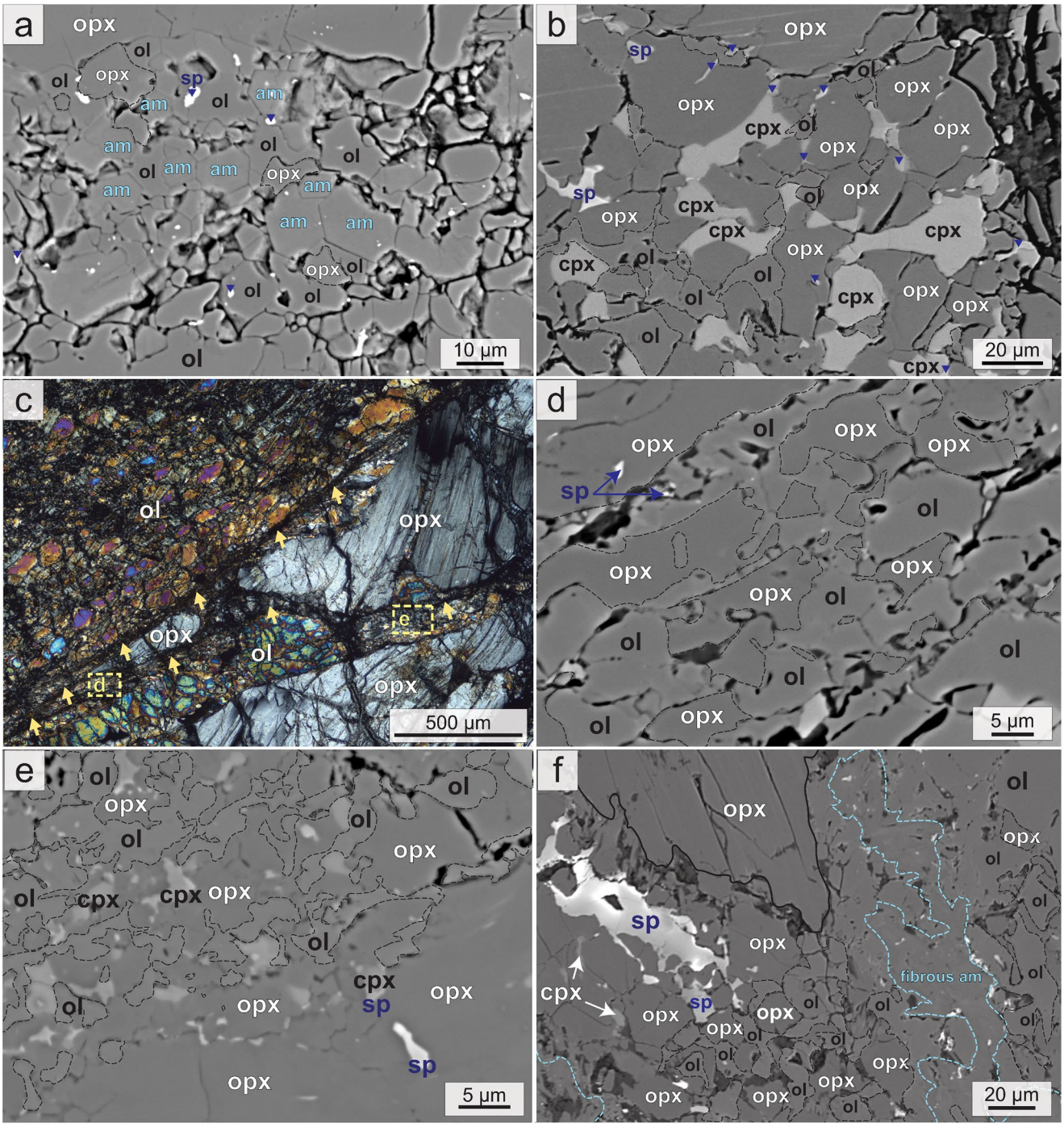

Figure 8. Microphotograph and SEM images of GSR zones in textural type A2 and A3 samples. (a) SEM image of sample SMS-DR17-4-6 (textural type A2). Mineral assemblage in GSR zone comprises irregularly shaped to polygonal orthopyroxene (opx), polygonal to interstitial olivine (ol), polygonal amphibole (am) and rare spinel neoblasts (sp, dark blue arrows). (b) SEM image of sample SMS-DR10-4-13 (textural type A3) away from the GSR zones. Mineral assemblage is composed of coarser polygonal orthopyroxene (opx) with interstitial to polygonal clinopyroxene (cpx), interstitial olivine (ol, grain boundaries in dashed black contours) and spinel (sp, dark blue arrows). (c) Microphotograph (polarized light) of the same sample. GSR zones (yellow arrows) developed near coarse orthopyroxene (opx) grains with undulose extinction and kink bands. (d) SEM image (yellow box in c). Mineral assemblage in GSR zone comprises polygonal to interstitial olivine, irregularly shaped clasts of orthopyroxene (dashed lines), and occasional spinel neoblasts. (e) SEM image (yellow box in c). Mineral assemblage in GSR zone comprises irregularly shaped to polygonal orthopyroxene (opx), polygonal to interstitial olivine, clinopyroxene (cpx) and very small spinel (sp) neoblasts. (f) SEM image of sample SMS-DR10-4-8 (located in Figure 7b). Mineral assemblage in GSR zone comprises irregularly shaped to polygonal orthopyroxene (opx), polygonal to interstitial olivine, polygonal clinopyroxene (cpx) and spinel neoblasts. Note the irregularly shaped spinel porphyroclasts. A vein filled with undeformed fibrous amphibole crosscuts the GSR zone.

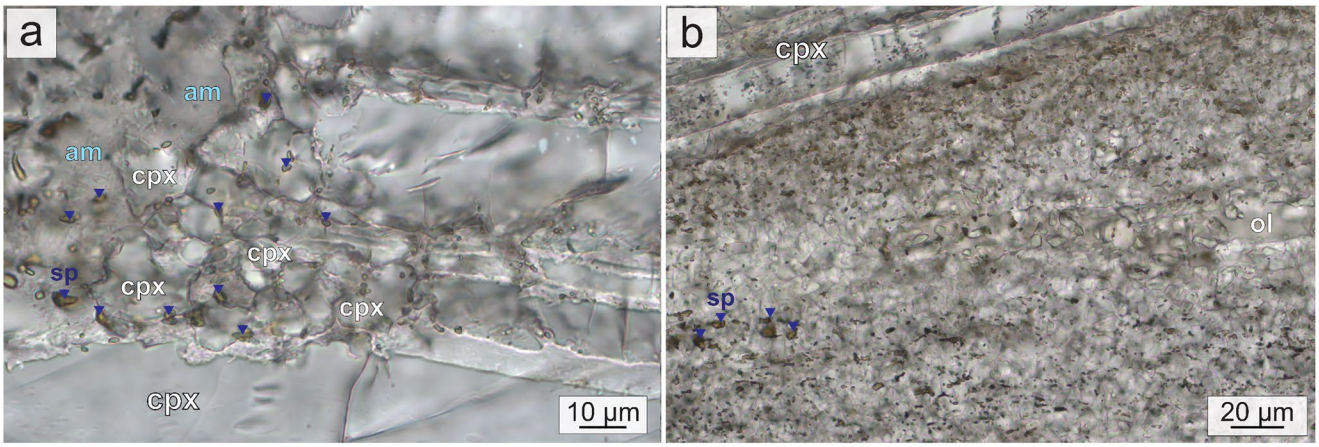

Figure 9. Crossed-nicols microphotographs of a late and extensively altered GSR zone in a spinel and clinopyroxene-rich domain (Figure 7e). Sample SMS-DR10-4-8 (textural type A3). (a) The mineral assemblage is more preserved close to clinopyroxene porphyroclasts, and comprises polygonal clinopyroxene (cpx) and small rounded spinel (sp) neoblasts. Away from the porphyroclast, late amphibole obscures the original recrystallized assemblage. (b) In more altered zones, µm-sized spinels are altered into magnetite and outline pseudomorphs of the original pyroxene and olivine (ol) neoblasts, replaced by post-kinematic hydrous minerals (mixtures of serpentine, chlorite and actinolitic amphibole).

commonly forming tails of neoblasts next to sigmoïdal-shaped porphyroclasts (Figures 7e and S2). Clinopyroxene neoblasts are polygonal and spinel neoblasts are mostly interstitial (Figures 8f and 9a).

Later GSR zones (<1 mm-thick) with finer grains and more planar shapes locally crosscut or line the GSR zones in spinel and/or clinopyroxene-bearing domains (Figure 7e). These later GSR zones host significant postkinematic hydrous mineral alteration and iron oxides that obscure the initial mineralogical assemblage (Figure 9b). Partially preserved domains contain an assemblage of olivine, clinopyroxene, and spinel neoblasts (<5 µm) with a polygonal texture (Figure 9). Partly serpentinized olivine microporphyroclasts are also found within the fine-grained altered assemblage.

5. Crystal Preferred Orientations, Intragranular Deformation, and GSR Processes

5.1. Crystallographic Orientations of Coarse Olivine and Pyroxene Grains

We measured olivine and pyroxene CPO in 26 thin sections from 17 samples. Given the large difference in size between the olivine and pyroxene porphyroclasts (mm-to cm-sized) and neoblasts in the GSR zones (µm-sized), the former dominate the CPO patterns where the CPO is shown as one point per pixel. Moreover, the number of porphyroclasts analyzed in each sample is small, which might lead to an overestimation of the intensity of the CPO. The sampled volumes are not statistically representative even when multiple sections were analyzed.

In samples for which a single thin section was analyzed, pole figures show the orientation of <50 coarse olivine grains and a lesser number of coarse ortho- and clinopyroxene grains (Figures 10 and S3). The olivine CPOs are dominated by the orientation of the coarsest grains; pyroxene grains show no preferred crystallographic orientation. In samples for which multiple thins sections were analyzed (larger volumes, more representative), olivine has CPO with moderate intensity and either axial-[100] (Figures 11b, 11c, 11e, 11f) or axial–[010] patterns (Figures 11a and 11d). Olivine CPO for single measured thin sections is presented in Figure S3.

5.2. Intragranular Deformation of Coarse Olivine Grains in Textural Types A2 and A3 Samples

Intragranular deformation features in the coarse olivine grains of the more deformed samples (textural types A2 and A3) are heterogeneous at the thin section scale (Figures 12 and 14). We distinguish two types of coarse olivine grains: strongly kinked olivines and olivines with few or no visible kinks. In textural type

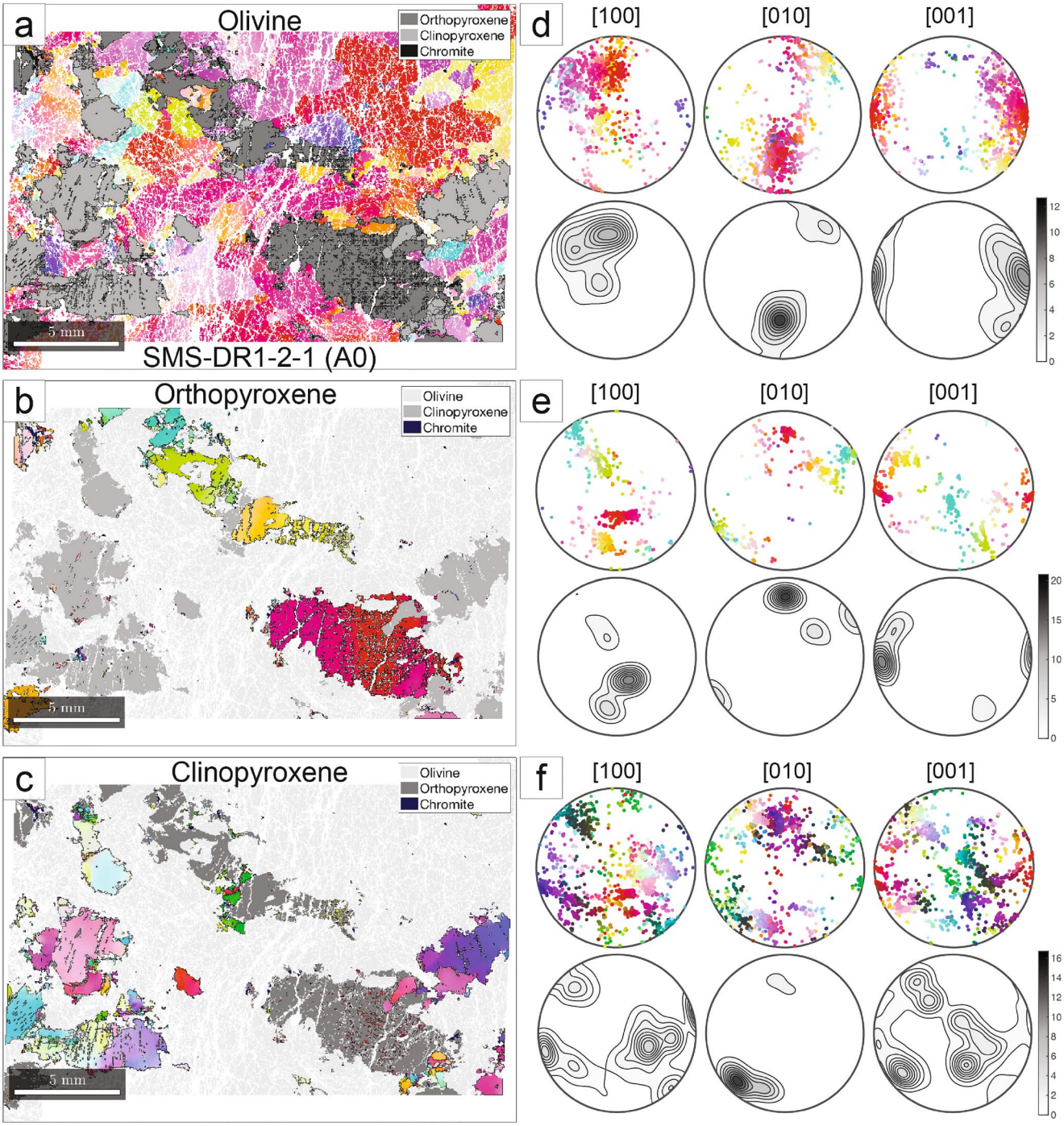

Figure 10. Textural type A0 EBSD maps (a–c) and (d–f) corresponding equal area lower hemisphere stereographic projections of the [100], [010], and [001] crystallographic axes of olivine, orthopyroxene and clinopyroxene in the EBSD map reference frame (long side of the map is E-W and short side is N-S in the pole figures) for the weakly deformed partially serpentinized sample SMS-DR1-2-1 (Figure 4a). Thin section was cut in a random orientation, since no foliation or lineation could be defined in the hand sample. EBSD pixel size is 35 × 35 μm. Colors in the EBSD maps correspond to the crystallographic orientations in the corresponding pole figures. (d–f) Upper panel of the pole figures represents all measured pixels for the corresponding mineral in the EBSD map, and the lower panel, density contours of the distribution at 1 multiple of a uniform distribution intervals.

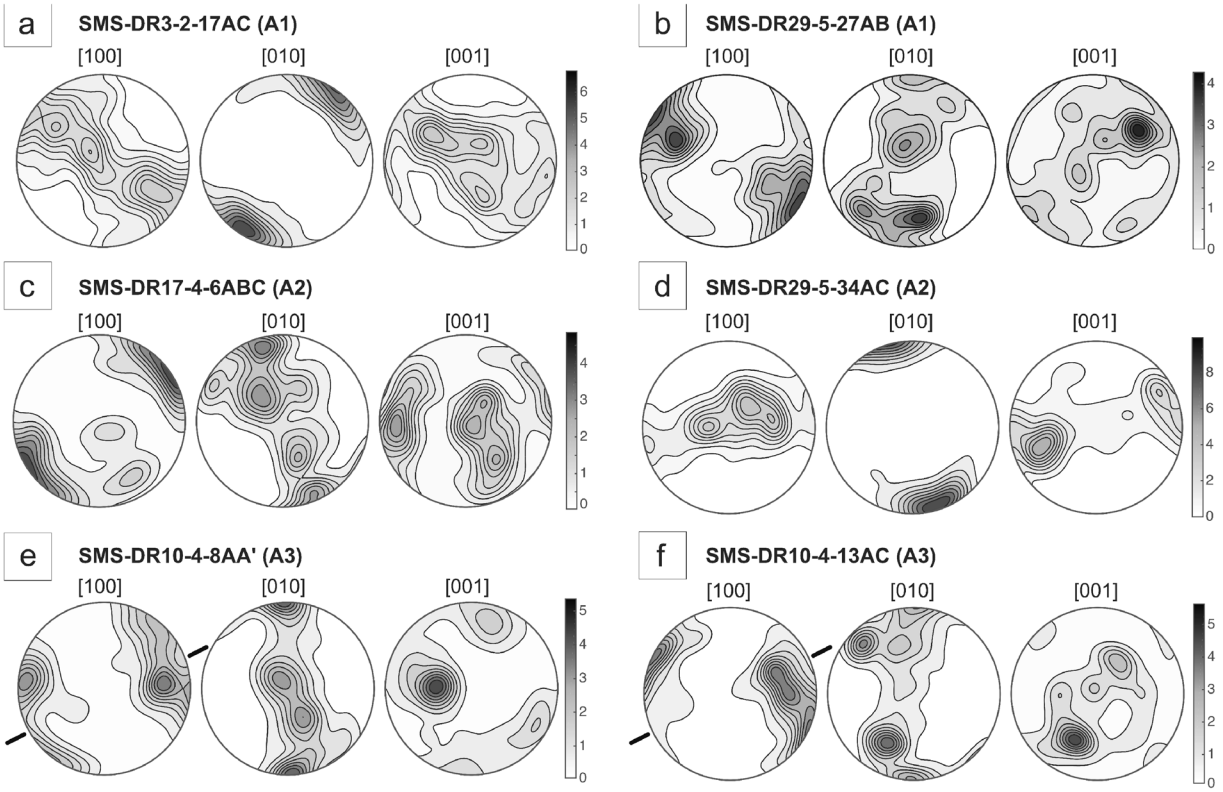

Figure 11. Equal area lower hemisphere stereographic projections of the [100], [010], and [001] crystallographic axes of olivine in partially serpentinized peridotite samples with textural types A1 (a - b), A2 (c - d), and A3 (e - f). EBSD pixel size is 35 × 35 μm. Pole figures are shown in density contours of the distribution at 1 multiple of a uniform distribution intervals. Due to the large olivine porphyroclast size, EBSD measurements were completed for each sample in two to three orthogonal thin sections: letters at the end of the sample name refer to thin sections analyzed. Sample number and textural type (in brackets) are shown in upper left for each CPO figure. (e - f) Small black lines indicate the trace of GSR zones for samples with textural type A3.

A2 samples, strongly kinked olivine grains are common. In those samples that display a preferred orientation of the trace of the GSR zones at the thin section scale, the trace of the kinks is preferably oriented at 5–20° to that of the GSR zones (Figure 12a). Strongly kinked olivines have their [100] crystallographic axes preferentially oriented sub-perpendicular to the trace of the GSR zones in the thin section and their [010] axis subparallel to this trace (Figures 12b and 12e). In contrast, coarse olivine grains that are not kinked have their [010] axis preferentially subperpendicular to the trace of the GSR zones, suggesting that their [100] axis may lie near the GSR planes (Figures 12c and 12d).

Kink bands result in sharp misorientations, with characteristic girdle dispersion patterns of the three main olivine crystal axes, indicating extreme intracrystalline misorientations (Figures 12b, 12e and 13b), which may attain 80° (Figure 13c). Kink bands are dominantly associated with rotations around the [001] axis (Figure 13b), but the presence of subgrains and undulose extinction within the kinked domains results in more complex orientation patterns, with all three axis forming girdles in the pole figures (Figure 12b). The kink bands are characterized by the sharp variation in orientation from blue to purple that is preferentially accommodated by a rotation around [001], whereas misorientations across subgrains within the kinked domains are mainly associated with rotations around [010] (variation in orientations from purple to pink in Figure 12b) and secondarily around [001] (variation in orientations from blue to green in Figure 12b). The misorientation angle varies continuously both along a kink boundary and among different kink boundaries in the grain (Figure 13c).

In textural type A3 samples, most coarse olivine grains are porphyroclasts with a strong shape preferred orientation, which results from the distribution of the GSR zones that crosscut originally coarser olivine grains (Figures 7d and 14a). Strongly kinked olivine grains are only observed in the least deformed parts of these samples (Figure 7c). The porphyroclasts in and next to GSR zones are moderately kinked and their

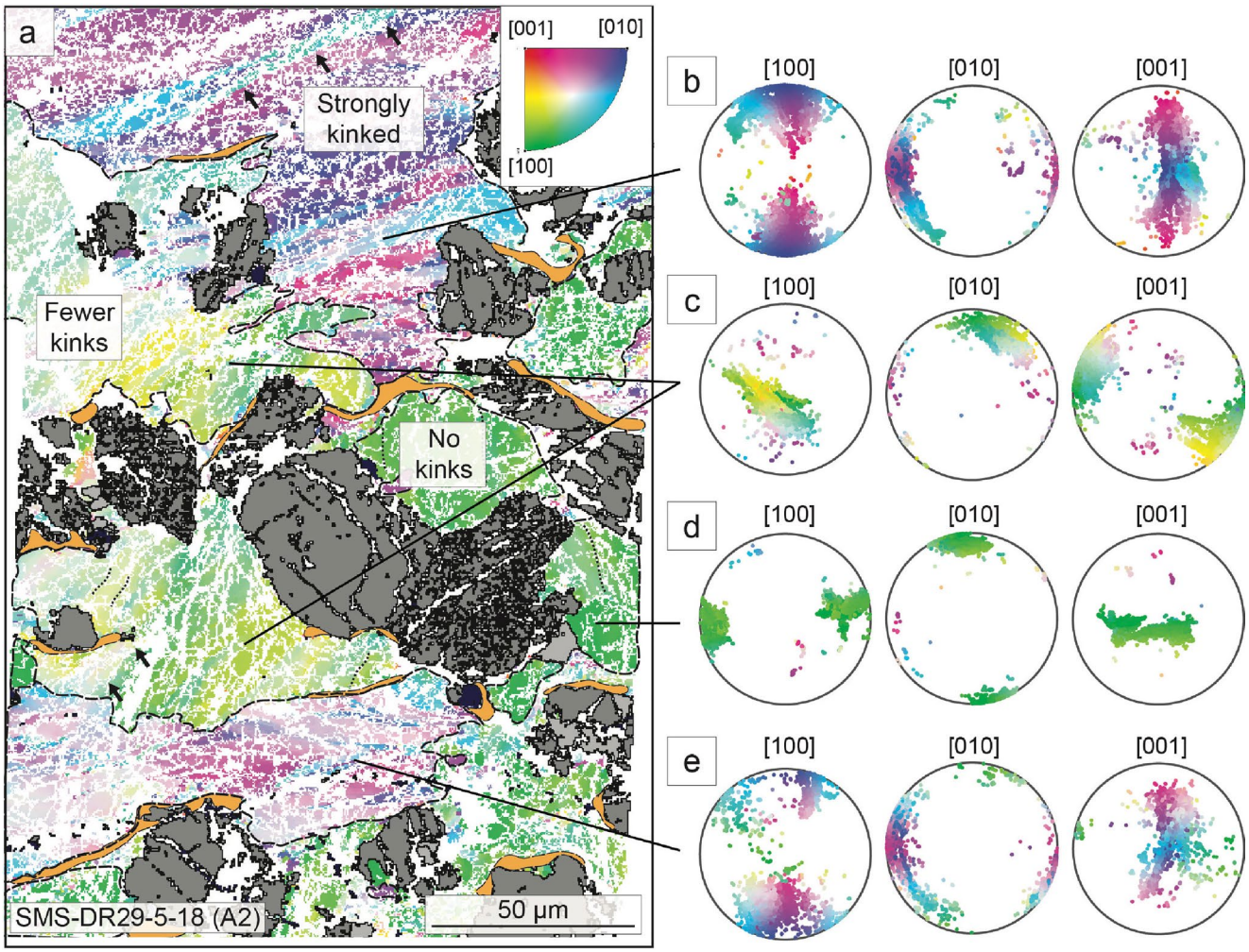

Figure 12. Olivine intragranular deformation in textural type A2: (a) EBSD map and (b–e) equal area lower hemisphere stereographic projections (in the EBSD map reference frame) of the [100], [010], and [001] crystallographic axes of large olivine grains in sample SMS-DR29-5-18. EBSD pixel size is 35 × 35 μm. Inverse Pole Figure (IPF, long axis of the map) color key is shown at the top right of the EBSD map. In (a) orthopyroxene is displayed in dark gray, clinopyroxene in light gray, spinel in dark blue, and GSR zones in orange. GSR zones are preferentially oriented perpendicular to the EBSD map plane; their trace is sub-horizontal. Large olivine grains display kink bands (black arrows) and subgrain boundaries (black dashed lines). (b–e) Pole figures present all measured pixels for each corresponding olivine grain. Two types of olivine grains are distinguished, based on their CPO and degree of kinking: olivine grains with their [100] axes at high angle to the GSR zones (blue-purple) are strongly kinked (b and e), while those that have their [100] axes at low angle to the GSR zones (green-yellow; c and d) display moderately disoriented (100) subgrain boundaries and are not (or weakly) kinked.

kink bands trend near parallel to the trace of GSR zones (as in the lower portion of porphyroclast P2 in Figure 14a). Due to the very coarse grained nature of the protolith, the thin section is not a representative volume and at this scale, olivine porphyroclasts do not show a CPO. For instance, porphyroclasts P1, P2, and P3 in Figure 14a display clearly distinct crystallographic orientations. The pole figures illustrating the intragranular misorientation in these three porphyroclasts have, however, a common characteristic: the [100] and [001] axis form girdles around the [010] axis. This pattern of intragranular misorientation is related to the combination of undulose extinction and an orthogonal pattern of (100) and (001) tilt boundaries that produce a patchy undulatory extinction pattern (see details of porphyroclasts P1 and P2 in Figures 14b and 14d). (100) and (001) subgrain boundaries are more closely spaced, and accommodate more distortion in regions of the porphyroclasts that have their [100] axis perpendicular to the GSR trace (Figure 14d). These intragranular misorientations locally result in formation of subgrain cells of variable sizes as a function of the grain orientation and proximity to the GSR zones: 80–100 μm in the porphyroclast P1, far from any GSR zone (Figures 14b) and 30–50 μm in the vicinity of the GSR zone that crosscut the porphyroclast

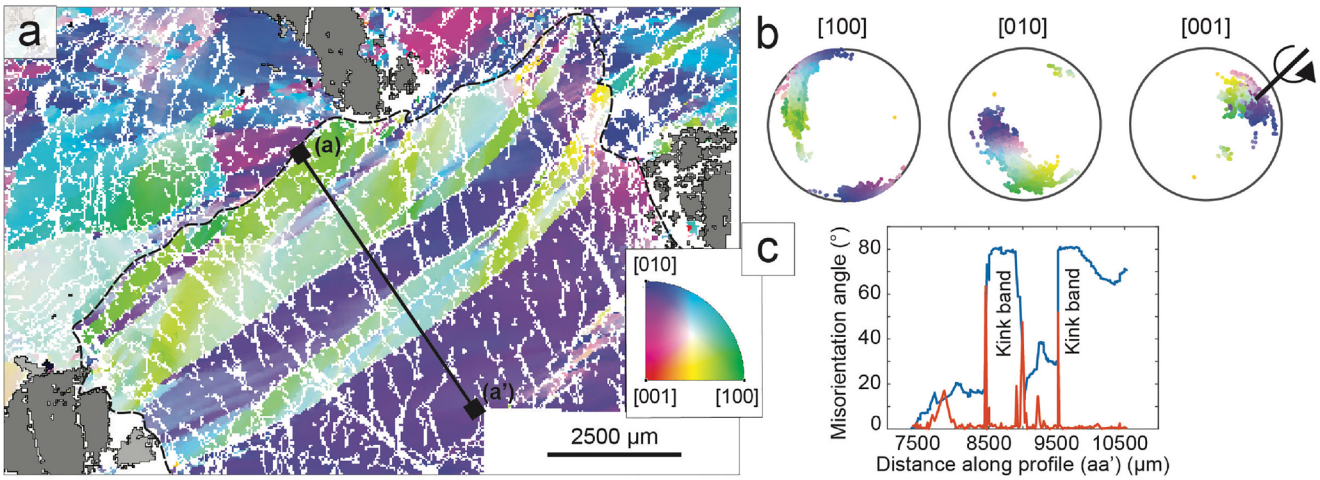

Figure 13. Kink bands in textural type A2: (a) EBSD map, (b) equal area lower hemisphere stereographic projections (in the EBSD map reference frame) of the [100], [010], and [001] crystallographic axes of a large kinked olivine grain, and (c) misorientation profile crosscutting the kink bands for deformed sample SMS-DR17-4-6 (see location of the map in Figure 5a and corresponding sketch in Figure 5b). EBSD pixel size is 35 × 35 µm. Inverse Pole Figure (IPF, long axis of the map) color key is shown at the bottom right of the EBSD map. Orthopyroxene is displayed in dark gray, clinopyroxene in light gray. In (c) the blue curve shows the misorientation relative to the first point of the profile (aa') and the red curve the misorientation relative to the neighbouring pixel.

P2 (Figures 14c and 14d). The subgrain cells coexist with isolated neoblasts with similar sizes and elliptical shapes, more frequent adjacent to the GSR zones (Figures 14b and 14c).

5.3. Microstructures and CPO in the GSR Zones

In textural types A2 and A3, olivine-rich GSR zones (Figure 14) and polymineralic GSR zones along orthopyroxene porphyroclasts (Figure 15) display distinct microstructures, implying different mechanisms of formation.

The olivine-rich GSR zones contain two types of olivine grains: elongated and smaller equant neoblasts (Figures 14b–14d). Elongated neoblasts are 2–30 µm long, <10 µm wide. They are elongated either parallel, or at a moderate angle (<45°) to the trace of the GSR zones. In the latter case, this angle is similar to the angle between the trace of the GSR zones and the preferred orientation of (100) subgrain boundaries in nearby porphyroclasts (Figures 14b and 14c). The smaller, equant neoblasts are less than 10 µm in size on average (Table S4 and Bickert et al., 2020). Neoblasts in olivine-rich GSR zones have a similar, but more dispersed, CPO as the adjacent porphyroclasts (Figure 14a). The dispersion of the CPO increases with distance from the porphyroclast (Figure 14c). Both types of neoblasts are interpreted as formed by dynamic recrystallization by subgrain rotation, based on their similarity to the subgrain cells in the adjacent porphyroclasts and on the progressive misorientation relative to the parent porphyroclast.

In contrast, polymineralic GSR zones developed along orthopyroxene grain boundaries contain domains mainly composed of small (<10 µm) neoblasts of olivine and domains composed of intermixed olivine and pyroxene crystals with irregular shapes and more variable sizes (Figures 15a–15c). Small prismatic amphiboles are dispersed in both domains. Interphase boundaries between olivine and pyroxenes are contorted, with marked interpenetrations (Figures 8b and 8e). Other features of polymineralic GSR zones include: (i) development of a faint compositional banding marked by the alignment of small elongated orthopyroxene grains subparallel to the GSR zone trend (Figure 15b); and (ii) common cusp-shaped terminations of small clino- (Figures 8b and 8e) and orthopyroxene grains (Figure 15b). Spinel porphyroclasts also display internal misorientation (Figure 15c) that defines subgrain cells of various sizes, locally with tails of recrystallized spinels (Figure 15c). Both olivine and orthopyroxene neoblasts show a highly dispersed CPO; only part of the neoblasts display similar orientations to the neighboring porphyroclasts (Figures 15d and 15e). The amphiboles display a weak CPO characterized by alignment of [100] parallel to the GSR zone trace (Figure S4).

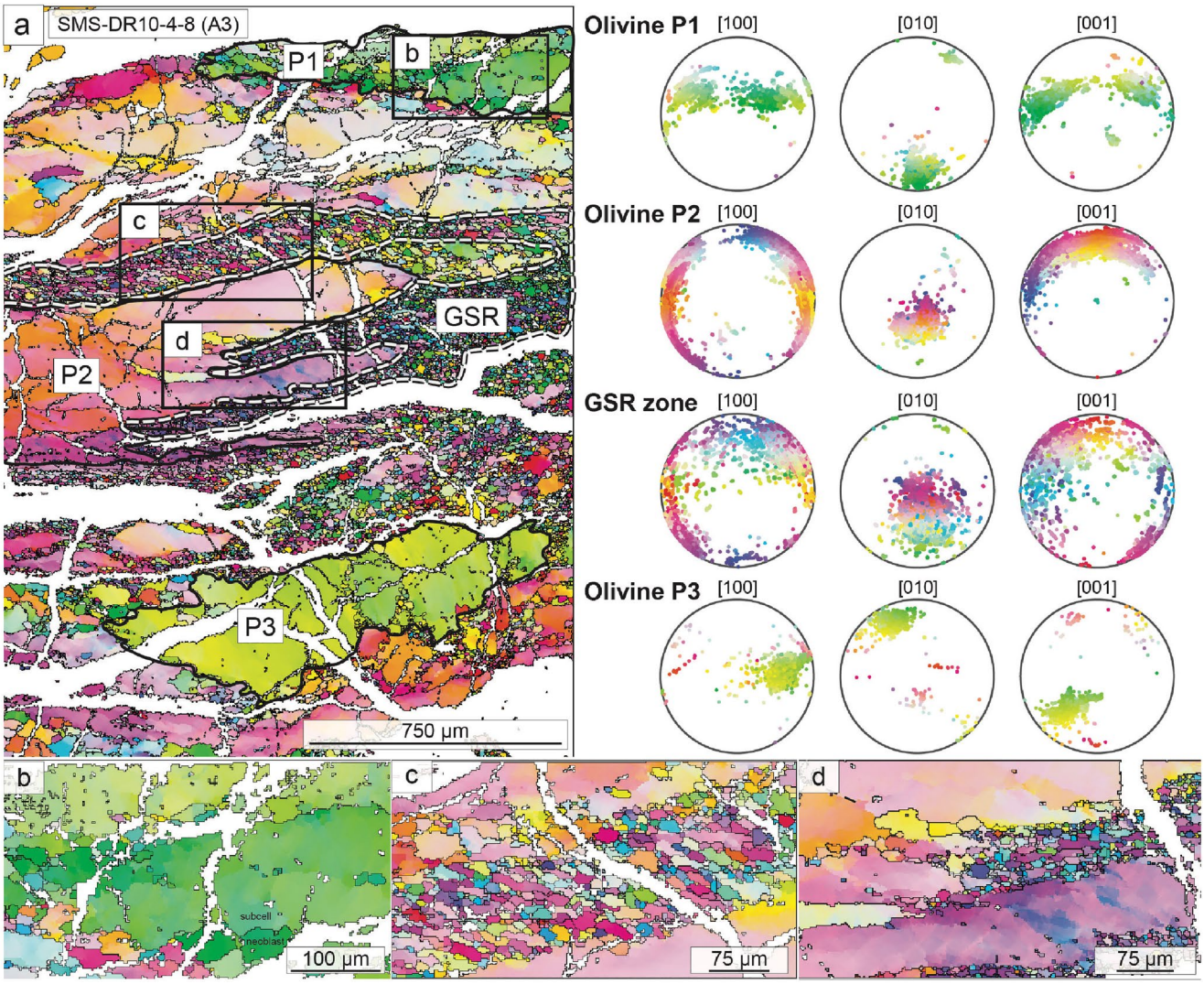

Figure 14. Textural type A3: EBSD maps and equal area lower hemisphere stereographic projections (in the EBSD map reference frame) of the [100], [010], and [001] crystallographic axes of olivine in highly deformed sample SMS-DR10-4-8. The thin section is cut perpendicular to the GSR zones but we were not able to determine the lineation. (a) EBSD map (located in Figure 7d) and olivine CPO for three olivine porphyroclasts (labeled P1, P2, and P3) and the anastomosing GSR zone next to olivine P2 (outlined with dashed white line and labeled GSR). EBSD pixel size is 2 × 2 µm. (b–d) are high-resolution EBSD maps: (b) Patchy CPO domains in olivine porphyroclast P1, with sub-orthogonal subgrain boundaries; (c) Detail of the GSR zone that cuts into olivine porphyroclast P2, which comprises two types of grains: (1) grains with an apparent elongation oblique to the GSR zone trend and crystallographic orientations similar to that of porphyroclast P2, and (2) smaller equant neoblasts with more variable crystallographic orientations; (d) Another detail of the GSR zone that cuts into olivine porphyroclast P2, which presents a patchy extinction pattern forming orthogonal subgrain cells. The GSR zone terminates in a horse-tail structure within P2, with thin recrystallization bands that appear to develop along former kink bands or subgrain walls.

Recrystallized olivine grain sizes are similar in olivine-rich and in polymineralic GSR zones (Table S4). This observation differs from previous works that identified smaller olivine grain sizes in polymineralic relative to monomineralic recrystallized domains and interpreted this observation as resulting from grain growth inhibition by the other phases (Cross et al., 2017; Herwegh et al., 2011; Linckens et al., 2011, 2015; Warren & Hirth, 2006).

6. Discussion

Our observations indicate that the deformation of the axial mantle in nearly amagmatic SWIR spreading corridors, below the domain affected by extensive hydration and associated serpentinization, is highly heterogeneous. This deformation is mainly accommodated by viscoplastic processes (dislocation creep,

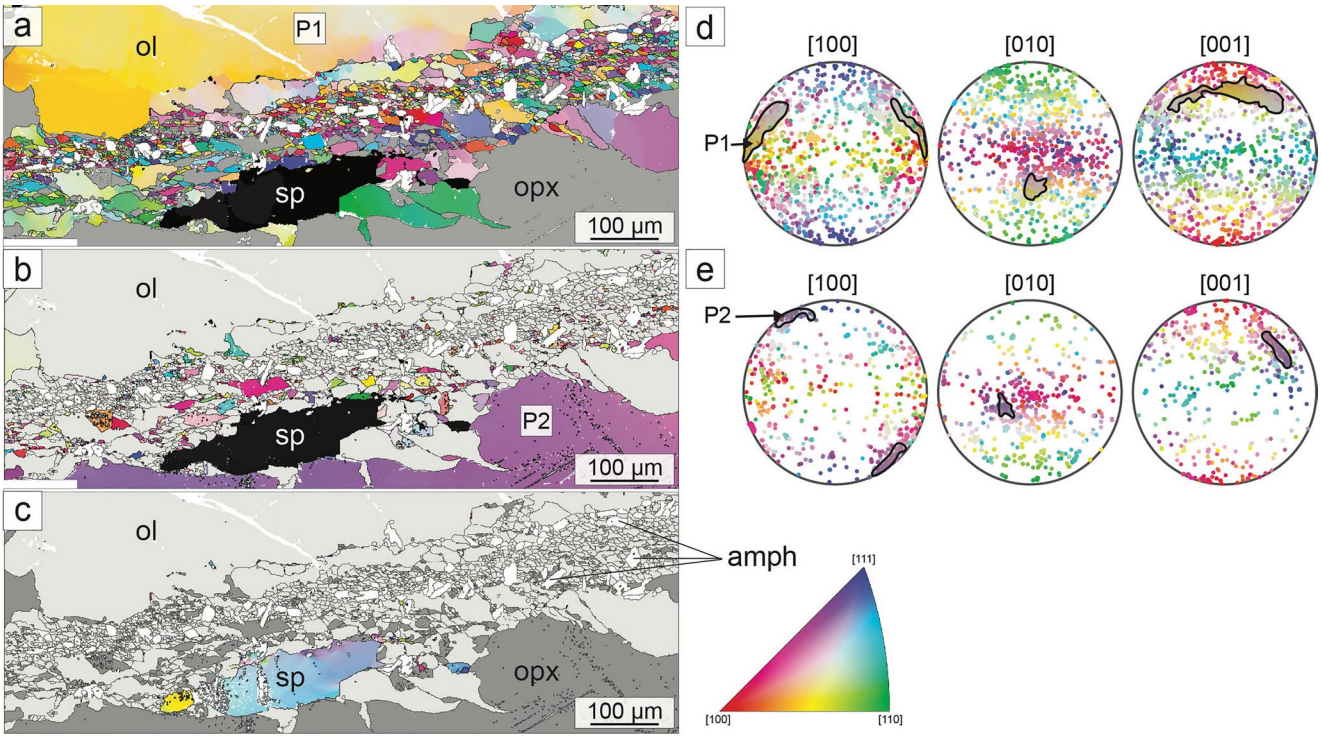

Figure 15. EBSD crystal orientation maps (a–c) and equal area lower hemisphere stereographic projections (d and e; all measurements plotted as one point per pixel) in the EBSD map reference frame of the [100], [010], and [001] crystallographic axes of olivine (d) and orthopyroxene (e) for a thin GSR zone at the contact between orthopyroxene and olivine in sample SMS-DR17-4-6 (textural type A2). EBSD pixel size is 1 μm^2. (a) Crystal orientation map for olivine (ol); orthopyroxene (opx) is in dark gray, amphibole in white (with black contours) and spinel (sp) in black. The olivine porphyroclast shows a pattern of sub-orthogonal subgrain boundaries close to the GSR zone. (b) Crystal orientation map for orthopyroxene (opx); in contrast to the olivine porphyroclast P1, the large orthopyroxene porphyroclast P2 does not display subgrains; small orthopyroxenes in the GSR zone are dominantly elongated parallel to the trend of the zone. (c) Crystal orientation map for spinel (color code as in the inverse pole figure of the long axis of the map); olivine (ol) is in light gray, orthopyroxene (opx) in dark gray, and amphibole in white. The spinel porphyroclast shows undulose extinction and subgrain cells toward the center of the GSR zone. (d and e) Pole figures present all measured pixels of the EBSD map for (d) olivine grains and (e) orthopyroxene grains. Contoured domains indicate the orientation of the olivine porphyroclast P1 (in a) and the orthopyroxene porphyroclast P2 (in b).

dynamic recrystallization, and formation of kink bands in olivine), but brittle processes (microfractures) are also activated. Strain and stress focusing results in the formation of anastomosed networks of GSR zones. The intensity of deformation varies between and within individual samples, but the deformation is ubiquitous across the sample suite (Table 1). In this section, we discuss: (1) the mechanisms and the conditions of the deformation; and (2) the possible settings for deformation in the context of nearly amagmatic, detachment-dominated ridge spreading. We also compare the present observations with the deformation of peridotite samples recovered in the footwall of detachments in mid-ocean ridges with a stronger magmatic activity and in extensional shear zones of orogenic peridotite massifs.

6.1. Mechanisms and Conditions of the Deformation

Coarse olivine crystals display variable degrees of intracrystalline deformation, ranging from: (1) undulose extinction in type A0 sample (Figure 4a); (2) subgrain boundaries and kink bands, which density increases from A1 to A3 types (Figures 4–7); and (3) closely spaced polygonal subgrains producing a patchy extinction pattern, which evolves by subgrain rotation recrystallization to form the olivine-rich GSR zones in A2 and A3 type samples (Figures 5–9). The misorientations associated with the undulose extinction and planar subgrain boundaries in coarse olivine crystals correspond primarily to rotations around [010] and [001] (cf. pole figures in Figures 12b–12e, 13b, and 14a), and subgrain boundaries are dominantly parallel to (100). Both indicate activation of [100] glide, mainly on the [010] and [001] planes. (001) tilt subgrain boundaries are also common in the vicinity of GSR zones. They mark the activation of the high stress [001] glide (several hundreds MPa; Carter & Avé Lallemant, 1970; Demouchy et al., 2013; Durham & Goetze, 1977; Matysiak

& Trepmann, 2012), which is consistent with the high differential stress values estimated from recrystallized grain size piezometry (80–270 MPa, Bickert et al., 2020 and Table S4) and with the presence of kinked olivines (Figures 5a–5c, 5e, 12a and 13a). In experiments, at strain rates of 10^{-5} s^{-1}, the transition between dominant [100] and [001] glide occurs around 1,000°C (Demouchy et al., 2013; Durham & Goetze, 1977). At geological strain rates, this transition likely occurs at lower temperatures. Natural peridotite mylonites deformed at temperatures ≤900°C show olivine CPO implying dominant [100] glide (e.g., Frets et al., 2014; Hidas et al., 2016; Jaroslow et al., 1996; Precigout et al., 2007). In the present study, the predominance of (100) tilt walls in the porphyroclasts and the common observation of (001) walls in the vicinity of GSR zones indicate that deformation and recrystallization started in the dominant [100] glide field and that local stress concentrations resulted in activation of both glide directions. This predominance is also consistent with equilibration temperatures between 800 and 1,000°C obtained by pyroxene thermometry in polymineralic GSR zones (Bickert et al., 2020). Temperatures >820°C were also proposed for the formation of similar GSR zones, as reported by Chatzaras et al. (2020).

Kinks bands are common features in coarse olivine crystals in samples characterized by textural types A1–A3 in this study. In contrast, they are rare in naturally deformed peridotites from mid-ocean ridges and from peridotite massifs and xenoliths (e.g., Basu et al., 1977; Boudier & Coleman, 1981; Chatzaras et al., 2020; Jaroslow et al., 1996; Le Roux et al., 2008; Raleigh, 1968). One documented exception is the low-temperature centimeter-to meter-scale shear zones in the Finero massif (Alps; Matysiak & Trepmann, 2015). Kink bands in olivine were also observed in Mg_2GeO_4 olivine deformed experimentally under relatively high pressure (0.6–1.3 GPa) and high stress conditions (1.3–2.5 GPa; Burnley et al., 2013) and in coarse-grained peridotites deformed in axial extension (Ben Ismail et al., 2020). These kink bands share many characteristics with those observed in the present study, in particular the very strong and highly variable misorientations along the kink boundary (up to 70°) and a consistent rotation axis. However, in the experimental study on Mg_2GeO_4 olivine the kink planes traces were roughly normal to [001] and the rotation axis accommodating the misorientation is [010], suggesting that the [001](100) dislocation glide system contributed to their formation (Burnley et al., 2013). In the present study, in the Finero peridotite mylonites, and in experimentally deformed peridotites, kink bands commonly have planes at low angle to (100) and rotation axes close to [001], indicating a strong contribution of dislocations of the [100](010) system to their formation (Figures 12a and 13b). The activation of different slip systems for formation of kink bands in the Burnley et al. (2013) experiments may be explained by the different composition (germanate vs. silicate). In all cases, kink bands develop in crystals with high mechanical anisotropy, when they are stressed in orientations that are not favorable for dislocation creep (Burnley et al., 2013; Raleigh, 1968). This result is consistent with our observation that kink bands develop in olivine crystals that have their [100] axis at a high angle to the trace of the GSR planes (Figure 12a). Our interpretation is that kink bands developed in those crystals because they were not favorably oriented relative to the imposed stresses to deform by dislocation glide. The very large misorientations (up to 80°) associated with the kink bands in olivine in our samples and in the two experimental studies, suggest that the deformation in the kink bands is probably locally accommodated by microfractures, in addition to dislocations. Cracks assisting strain accommodation in kink bands with high misorientations (>50°) were observed by TEM in highly anisotropic ceramics (Barsoum et al., 1999). In our samples, microfractures also develop in coarse olivine grains next to GSR zones, and are in some cases lined with small recrystallized grains (Figures 6c and 6d). These point to a complex interplay between crystal-plastic mechanisms, which are dominant at the thin section and sample scales, and limited amounts of brittle deformation.

Several observations suggest that the GSR zones initiated, at the cm-scale, adjacent to large orthopyroxene grains. These orthopyroxene grains are commonly kinked, which is consistent with their large mechanical anisotropy (Ross & Nielsen, 1978). However, these kinked orthopyroxenes are observed in all samples, including the least deformed ones, and can be shown in a few samples to predate the growth of coarse olivine grains (Figure 4a). We therefore interpret them as early crystal-plastic deformation features, predating the high stress deformation episode. During this latter deformation, large orthopyroxene grains are commonly fractured (Figures 4–7). Following Jammes et al. (2015), we propose that the contrast in mechanical behavior between the strong and brittle coarse orthopyroxene and the dominantly crystal-plastic surrounding olivine, explains the initial localization of the GSR zones at the centimeter-scale (Figures 5b, 5e, 6b, 7, and 12). High strength contrasts, leading to significant differences in mechanical behavior and to localized

stress concentrations at the millimeter-to-centimeter-scale, also resulted from the weak CPO and large grain sizes of the coarse olivine: poorly oriented olivines were kinked while dislocation glide prevailed in more favorably oriented olivines. GSR zones also often developed at the contact or within kinked olivine crystals; in the latter case, they follow the kink planes (Figures 6c, 6d, and 12).

We propose dynamic recrystallization by subgrain rotation as the main mechanism of GSR in olivine-rich GSR zones. This interpretation is consistent with several observations: the patchy extinction pattern in olivine porphyroclasts; subgrain tilt walls formed by the activation of nearly orthogonal glide systems within the crystal ([100](0kl) and [001](kh0); Figure 14); the similar sizes and shape of subgrains in the porphyroclasts and neoblasts in the GSR zones; the preservation of ribbon-shaped fragments of the original porphyroclasts within anastomosing GSR zones; and the weak CPO of neoblasts, which is nevertheless inherited from the adjacent olivine porphyroclasts (Figure 14).

The MDZs described by Chatzaras et al. (2020) share many characteristics with the GSR zones in the present study: they also formed by strain localization at high temperature (818–1,070°C) and record high, yet lower, differential stresses (22–81 MPa). Chatzaras et al. (2020) interpreted these MDZs to initiate as brittle deformation zones, associated with seismic events, which were subsequently overprinted by post-seismic viscous deformation that produced reequilibration of the microstructure by recrystallization. A similar interpretation had been proposed for microshear zones characterized by extreme grain size refinement in Alpine peridotites (Matysiak & Trepmann, 2012, 2015). However, in the present study, we do not observe evidence of an initial brittle deformation guiding the GSR zones; instead, the distribution of GSR zones is clearly controlled by the vicinity of pyroxene porphyroclasts (Figures 5a, 5b, 6a, and 6b) and kinked olivines (Figures 6c, 6d, 12a, and 14a). Microfracturing is local and also seems controlled by the strength heterogeneity of the grains composing the peridotite. Stresses estimated based on recrystallized grain sizes (80–270 MPa) are higher than those inferred in the MDZs from the Bogota Transform. Preservation of small grain size (1.5–84 μm) may result from rapid exhumation after deformation and recrystallization (Matysiak & Trepmann, 2015), which is more likely in an extensional than in a transform setting. Postseismic relaxation characteristic times are small relative to those associated with the activity of the detachment faults and we do not observe evidence for a peak in stress followed by a relaxation period. For these reasons, we do not interpret the GSR zones as initially formed by a brittle process (earthquake), although we cannot exclude that their formation may be favored by local stress increases just below the BDT, following earthquakes.

In polymineralic GSR zones, there is microstructural evidence for activation of dissolution-recrystallization processes in addition to dynamic recrystallization by subgrain rotation, such as: (i) the interpenetrating contacts between olivine and pyroxenes (Figures 8b, 8d–8f); (ii) the small elongated orthopyroxene grains with cuspate boundaries that form a faint compositional banding in several GSR zones (Figure 15b); and (iii) the interstitial shapes of clinopyroxene (Figures 8b and 8e). Such microstructures require the presence of fluids during deformation. More evidence for the presence of limited amounts of fluids during the formation of GSR zones is the occasional occurrence of polygonal to prismatic Mg-rich hornblende amphiboles (Table S3) in both olivine-rich and polymineralic GSR zones (Figures 8a and 15a–15c). These amphiboles display a weak CPO relative to the orientation of the GSR zones, suggesting syn- to late kinematic crystallization (Figure S4).

6.2. The Deep Root of Detachment Faults in a Nearly Amagmatic Mid-Ocean Ridge Setting

The lithosphere strength profile in Figure 16b is based on a hypothetical axial geotherm (Figure 16a) with a dominantly conductive (linear) gradient, as proposed by Cannat et al. (2019) for the SWIR in the nearly amagmatic 64°E region (Figure 1). The 800–1,000°C temperature range that corresponds to the high stress deformation documented in the peridotites is set to a minimum depth of about 18 km (0.6 GPa; Bickert et al., 2020). This minimum depth constraint is based on the observation of spinel and not plagioclase in the recrystallized assemblages and on the postkinematic character of plagioclase, which indicate that the deformation occurred in the spinel stability field (>0.6–0.8 GPa; Borghini et al., 2010). We use this geotherm to calculate the differential stress in the ductile regime using dislocation creep flow laws in olivine (Gouriet et al., 2019; Hirth & Kohlstedt, 2003; Karato et al., 1986) for two plausible strain rates (10^{-12} and 10^{-14} s^{-1}), consistent with plate spreading rates on the SWIR. In the brittle domain, we consider a coefficient of friction (μ) equal to 0.3 for serpentinized peridotites (Escartín et al., 1997) at temperatures <350°C (dominant

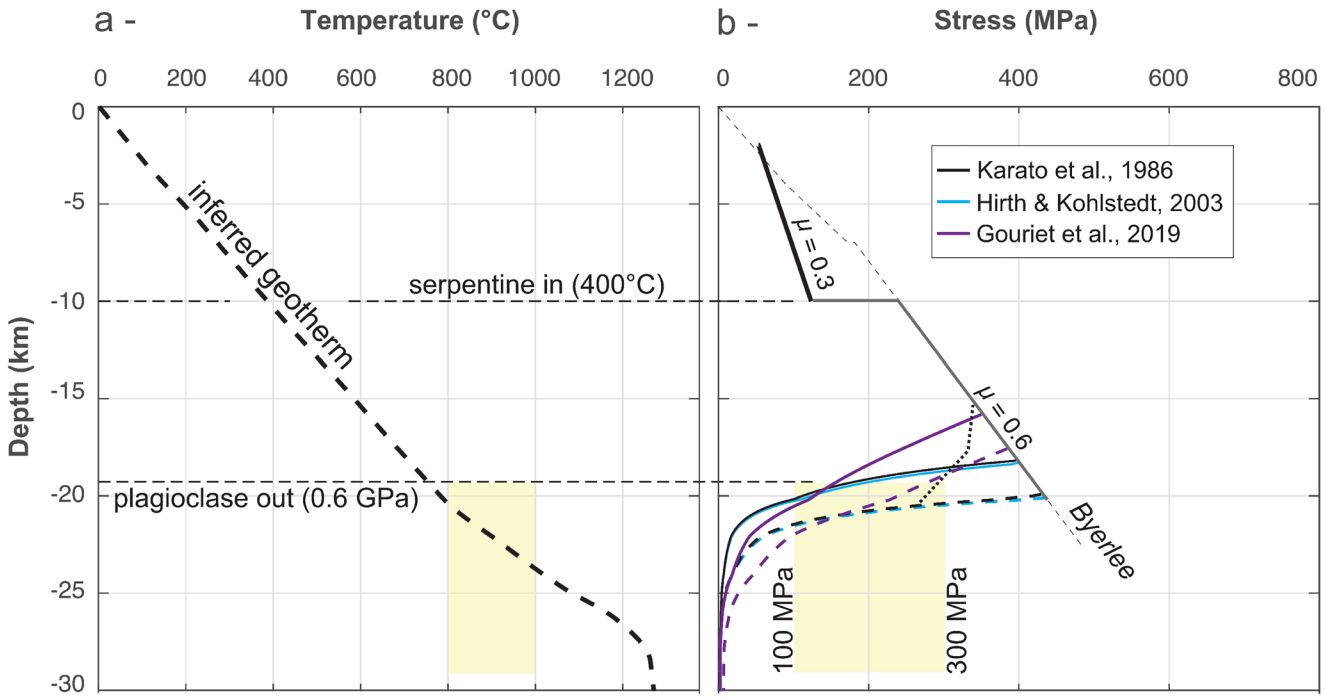

Figure 16. (a) Inferred geotherm and (b) corresponding strength envelope. (a) The geotherm is drawn in order to reach 800°C (the minimum temperature determined for GSR zones based on pyroxene geothermometers; see Bickert et al., 2020) at a depth of 20 km (the plagioclase-out depth for a fertile lherzolite composition; Borghini et al., 2010). (b) The strength envelope is built using Byerlee's law in the brittle lithosphere, but with a reduced friction coefficient at temperatures below 350°C (Escartin et al., 1997), and dry olivine dislocation creep flow laws (Karato et al., 1986, in black; Hirth & Kohlstedt, 2003, in blue; Gouriet et al., 2019, in purple) for strain rates of 10^{-12} (dashed lines) and 10^{-14} s^{-1} (continuous lines) in the ductile regime. Preliminary observations (Cannat et al., 2012) suggest that amphibole and chlorite-rich semi-brittle shear zones develop in hydrothermally altered samples at temperatures between 350°C and 800°C; the thick dash lines account for the effect of this process on the strength of the oceanic lithosphere. The yellow boxes correspond to the temperature and differential stress ranges determined for the GSR zones by Bickert et al. (2020).

serpentinization temperature in the peridotite samples; Rouméjon et al., 2015) and a $\mu = 0.6$ for temperatures higher than this isotherm. The resulting yield stress envelope (Figure 16b) predicts a BDT at depths of 18–20 km for dislocation creep laws of Karato et al. (1986) and Hirth and Kohlstedt (2003), and of 16–17 km for the Gouriet et al. (2019) flow law, consistent with the maximum earthquake depths recorded in the area (Chen et al., 2020).

The predicted strength of the axial lithosphere at the BDT in Figure 16b is similar in order of magnitude, but larger (~350 MPa using the Gouriet et al., 2019 flow law and ~400 MPa using the two other flow laws) than that estimated using recrystallized grain size piezometry for the GSR zones in the peridotites (up to 300 MPa). This difference could point to the coexistence of crystal-plastic and brittle mechanisms in a thick BDT zone. Seismic rupture on a detachment fault may occasionally increase the stresses in the shallowest ductile mantle (Ellis & Stockhert, 2004). Such events could initiate the high stress deformation described in this study. Mineral scale heterogeneity, such as between orthopyroxene and olivine, or between well and poorly oriented olivine crystals, produce local stress concentrations that focus strain and develop GSR by dynamic recrystallization, favoring fluid-related reactions. These processes would lead to localized weakening, which will help the active detachment to anchor in a domain of stable deformation—until continued spreading leads to development of a new detachment of opposite vergence (Bickert et al., 2020). We propose that the deformation documented in the dredged peridotites, at ~800–1,000°C and at maximum deviatoric stresses ~300 MPa, illustrates the mechanical behavior of the lithosphere toward the base of the BDT zone, in the root zone of the axial detachment faults formed in the context of a melt-starved ultraslow spreading ridge.

The context of this deformation is further explored in the conceptual sketches of Figure 17. We propose that the brittle and semi-brittle faults and shear zones forming the detachment, root into a system of

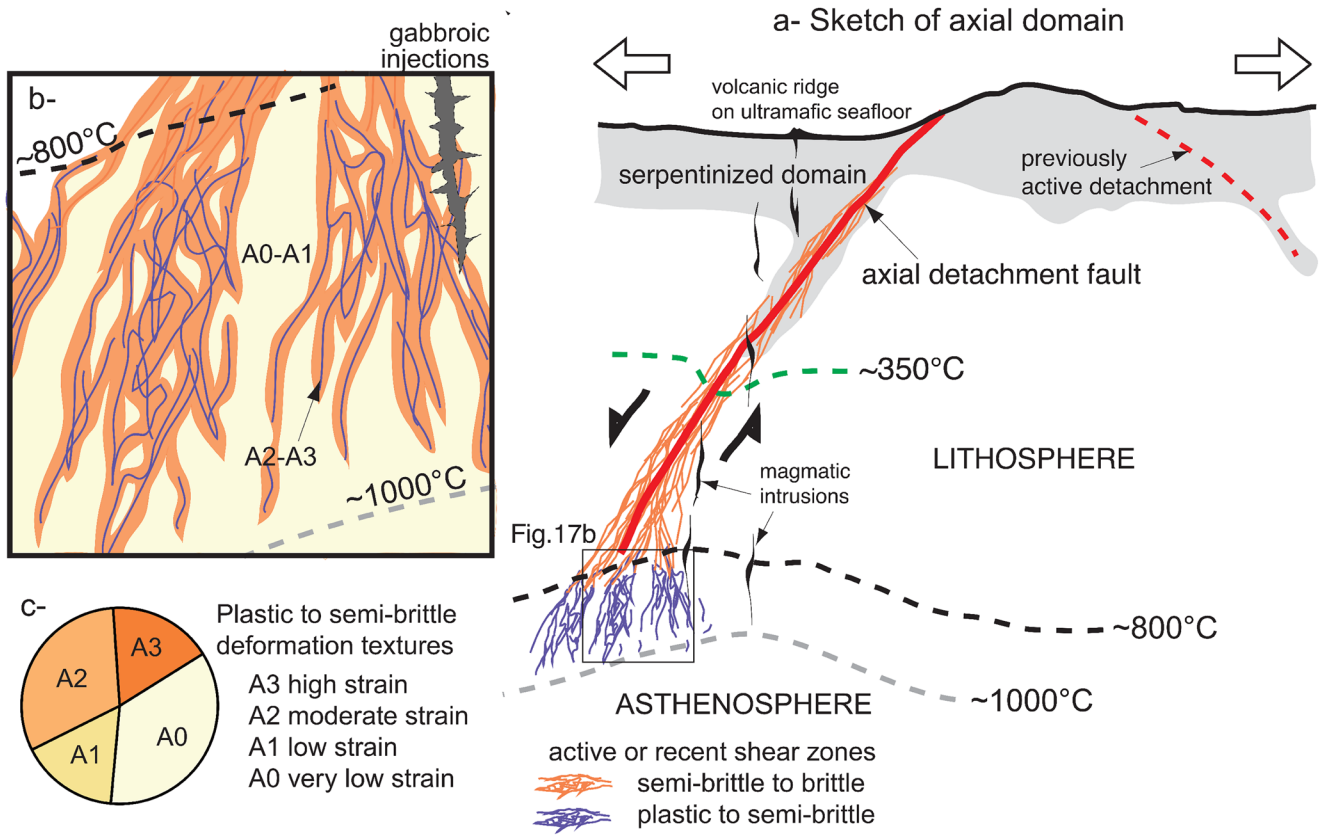

Figure 17. Schematic interpretations of the root of detachment faults at two scales: (a) macro- and (b) meso-scale. (a) Conceptual sketch of the root of a detachment fault in a nearly amagmatic corridor at the eastern SWIR (not to scale, redrawn from Cannat et al., 2019). The detachment roots into a domain of high-stress plastic to semi-brittle deformation heterogeneously distributed at the base of the lithosphere. (b) High strain zones form an anastomosing network, recorded as A2 and A3 textural types (in orange) that enclose less deformed areas (A0-A1 textures). (c) Proportion of the different textural types identified in the sample set of 99 partially serpentinized samples.

anastomosing, crystal plastic to semi-brittle shear zones. In this model, the most deformed peridotite samples (textural type A3) correspond to rocks deformed in these shear zones. We did not recover type A3 peridotites with GSR zones thicker than a few cm. While it is possible that dredging missed such samples or that the thicker GSR were completely reworked and retrogressed during the subsequent stages of the functioning of the detachment, it is also possible that the crystal plastic to semi-brittle shear zones sketched in Figure 17a are comprised of tightly spaced millimeter to a few centimeter-thick GSR zones such as in textural type A3 samples. The less deformed textural types A2, A1, and A0 would correspond to lenses surrounded by the anastomosed shear zone, which preserve the early stages of deformation associated with the detachment such as the microstructure and CPO resulting from a previous high-temperature, lower stress deformation (Figure 17b).

Although dredging might result in a biased sampling of the different microstructures, the proportion of textural type A0 (35%; Table 1 and Figure 17c) indicates significant strain localization. Dredge 10, collected in the axial region of the western nearly amagmatic corridor (Figure 1), contains solely samples with deformation textures A2 and A3. This abundance suggests that this dredge sampled one of the shear zones represented in Figure 17b, possibly several meters-thick or more, characterized by a higher density of GSR zones. In the other dredges, the proportion of type A3 is typically less than 20% (Table 1). We cannot ascertain that the present observations are representative of proportions of the different textural types at depth, but we used them to build the conceptual sketch presented in Figure 17.

The present study does not address the formation of the coarse-grained protolith (A0 texture). In samples with the A0 texture, kinked and locally recrystallized orthopyroxenes coexist with seemingly undeformed large olivine grains. The kinked orthopyroxenes also display embayments filled with olivine, a texture that

suggests incongruent melting (Dick et al., 2002; Seyler et al., 2007). These observations point to partial melting and olivine growth occurring after an earlier deformation, recorded by the pyroxenes intracrystalline deformation and by the CPO of coarse olivine grains. Mean temperatures calculated for the cores of pyroxene porphyroclasts are ≥1,110°C (Bickert et al., 2020). This deformation and the subsequent development of the coarse olivine grains may thus have occurred at the base of the lithosphere or in the upper asthenosphere beneath the ridge.

The GSR recrystallized assemblage locally contains Mg-rich polygonal hornblendes (Figure 8a; Table S3). Similar Mg-hornblende amphiboles formed at temperatures >800°C have been observed in peridotite samples from oceanic transform faults (Kohli et al., 2020; Prigent et al., 2020) and orogenic massifs (Vieira Duarte et al., 2020). In both cases, they were interpreted as derived from hydrothermal fluids that percolated down to the root of the faults. In samples that contain recrystallized amphiboles, we also find acicular to fibrous Mg-rich, Al and Ti-poor tremolites as postkinematic alteration of the GSR minerals, and in veins that crosscut the GSR zones (Figures 7 and 9; Cannat et al., 2012). The origin of the fluids that crystallized these tremolites is most likely hydrothermal and we propose, as a working hypothesis, that small quantities of these hydrothermal fluids percolated through the brittle and semi-brittle faults and shear zones forming the detachment, down to the plastic to semi-brittle root of the axial detachments, forming the polygonal hornblende in GSR zones (Figure 17a).

6.3. Comparison With More Magmatic Slow Spread Mid-Ocean Ridges and Extensional Shear Zones in Orogenic Massifs

Only a few partially serpentinized peridotite samples in our set are free of any imprint of the heterogeneous high stress deformation, which is in strong contrast with those sampled at the more magmatically active MAR. There, most abyssal peridotites have retained the high temperature, low stress deformation microstructures expected in the asthenospheric mantle or in the deep lithosphere, without any overprint of lower temperature high stress deformation (Achenbach et al., 2011; Ceuleneer & Cannat, 1997; Harigane et al., 2016; Seyler et al., 2007). The prevalence of high temperature low stress deformation indicates that, in more magmatically robust detachment-dominated slow spreading ridges, detachments likely root into magma-rich domains that are so weak that they localize the deformation and that the host mantle is mostly preserved from being deformed. This interpretation is supported by ample evidence for mylonitic deformation in gabbroic bodies and veins that intrude the exhumed peridotites (Cannat, 1991a, 1991b; Dick et al., 2002), forming a sizable proportion of the seafloor in corrugated oceanic core complexes (Ildefonse et al., 2007).

Ten percent of the partially serpentinized and variably deformed samples considered in this study host small amounts of plagioclase in the form of interstitial crystals or aggregates (Table 1), now altered into hydrous mineral assemblages (Figure S1). Even in highly deformed samples (textural types A2 and A3; Table 1), plagioclase is undeformed. Crystal-plastic deformation of plagioclase is also not observed in the more pervasively impregnated peridotite samples described by Paquet et al. (2016) and interpreted by these authors as associated with melts channeled episodically through the lithosphere to feed sparse eruptions at the seafloor. These observations suggest that the melt fractions were too low to localize detachment-related deformation and weaken the lithosphere.

Another difference between deformed partially serpentinized samples from the nearly amagmatic corridors of the eastern SWIR and those from most MAR detachment footwall locations is the olivine grain size. Olivine grains are commonly centimeter-sized in the SWIR sample set (Figure 4), while they are most commonly millimeter-sized in the MAR samples (Achenbach et al., 2011; Cannat et al., 1992; Ceuleneer & Cannat, 1997; Dick et al., 2010; Seyler et al., 2004). These centimeter-sized olivine grains in SWIR peridotites have irregular and lobate shapes, showing cuspate boundaries with orthopyroxene grains that could have resulted from incongruent melting (Dick et al., 2002; Seyler et al., 2007), which appears to postpone an early episode of kinking of the orthopyroxenes. This study does not provide robust constraints to discuss the geological context allowing for this partial melting and olivine grain growth. However, we propose, as a working hypothesis, that it could have occurred in the eastern SWIR flip-flop detachment context (Sauter et al., 2013), due to thermal rejuvenation of the lithosphere accreted in the footwall of a former detachment, as it is incorporated into the hanging wall of a more recent one (Cannat et al., 2019).

The detachment-related deformation documented here is also distinct from the deformation in extensional shear zones of orogenic massifs such as Turon de Tecouere, Ronda, Beni Bousera, Lanzo, or Totalp. Shear zones in these massifs are thicker (meters to kilometers-thick) and characterized by progressive strain localization under decreasing temperature conditions, forming mylonites and then ultramylonites at the expense of coarse-grained peridotites (Frets et al., 2014; Kaczmarek & Tommasi, 2011; Newman et al., 1999; Precigout et al., 2007). There is no interplay, as that recorded in the eastern SWIR samples, between microfractures and dynamic recrystallization (Figure 6). Moreover, recrystallized olivine in the mylonites are coarser (>50 μm, Frets et al., 2014; Kaczmarek & Tommasi, 2011), suggesting that stresses were lower during deformation. When very fine olivine grain sizes (<50 μm) are observed in polymineralic ultramylonites from orogenic massifs, their formation involves metamorphic reactions (Kaczmarek & Tommasi, 2011; Newman et al., 1999).

7. Conclusions

Along the eastern part of the SWIR, melt supply is very low and plate divergence is mostly accommodated by successive detachment faults that flip polarity. Analysis of deformation textures was performed in a set of 99 partially serpentinized peridotites dredged on and off axis along both flanks of the ridge. The samples provide evidence for a heterogeneous deformation that combines brittle and crystal-plastic deformation mechanisms and leads locally to extreme GSR, with formation of anastomosed networks of GSR zones. At the hand specimen and thin section scale, strain localization and deformation style appears to be controlled by:

- the strong rheological contrast between coarse orthopyroxene grains that deform by brittle processes and olivine grains that dominantly deform by crystal-plastic mechanisms, which explains the initial localization of GSR zones preferentially at contacts between olivine and orthopyroxene grains and between olivine crystals with contrasting orientations;
- the coarse grain sizes and variations in orientation of the olivine crystals relatively to the imposed stress. Kink bands develop in olivines that were not favorably oriented relative to the imposed stresses to deform by dislocation glide. The double activation of [100] and [001] glide systems, and the presence of kinked olivines, indicate high stresses;
- development of GSR zones by dynamic recrystallization by subgrain rotation in olivine rich-domains;
- the presence of small amounts of syn- to late kinematic amphibole in polymineralic GSR zones, indicating that small amounts of hydrous fluids circulate down to the root of the detachment;
- the large olivine grain size in the eastern SWIR samples is also an important parameter as it results in strong strain and stress heterogeneity at the cm-scale and in the formation of rare high-stress microstructures in olivine: kinks bands.

The intensity of this heterogeneous deformation varies between and within individual samples, but it is detected in nearly every sample, suggesting that this high-stress deformation episode affected a relatively large volume of the mantle below the axial detachment faults. We propose that the present microstructural observations illustrate the mechanical behavior of the lithosphere at the base of the BDT domain, where the detachment fault roots into a system of anastomosing, crystal-plastic to semi-brittle shear zones. It is noteworthy that primary minerals in abyssal peridotites collected in more magmatic slow-spreading ridge settings do not show this pervasive brittle-ductile imprint: there, melts likely control strain localization in the deep axial lithosphere.

Acknowledgments
The authors thank Basil Tikoff, an anonymous reviewer and the editor Whitney Behr for their helpful comments and suggestions. The authors acknowledge partial funding by ANR project «Ridge-Factory-Slow » (ANR-18-CE01-0002). Thanks to the IPGP Marine Rock Repository for sample curation. They are grateful to M. Quintin for providing the thin sections, to C. Nevado for high-quality polished thin sections for EBSD measurement, to D. Mainprice for the help with the MTEX scripts, and to F. Barou and M. Fialin for their technical assistance at the EBSD-SEM CNRS-INSU national facility at Géosciences Montpellier and at the CAMPARIS service in Paris, respectively. The IPGP SEM facility is supported by the IPGP multidisciplinary program PARI, and by Region île-de-France SESAME Grant no. 12015908. This is IPGP publication number 4192.

Data Availability Statement

The CPO and microprobe data on which the results of this work are based are available at the Zenodo Open AIRE repository under https://doi.org/10.5281/zenodo.4030433.

References

Achenbach, A. K., & Trepmann, C. A. (2012). Crystal-plastic deformation and recrystallization of peridotite controlled by the seismic cycle. *Tectonophysics*, *530–531*, 111–127. https://doi.org/10.1016/j.tecto.2011.11.029

Achenbach, K. L., Cheadle, M. J., Faul, U., Kelemen, P., & Swapp, S. (2011). Lattice-preferred orientation and microstructure of peridotites from ODP Hole 1274A (15°39′N), Mid-Atlantic Ridge: Testing models of mantle upwelling and tectonic exhumation. *Earth and Planetary Science Letters*, *301*(1–2), 199–212. https://doi.org/10.1016/j.epsl.2010.10.041

Agrinier, M., Mével, C., & Stakes, D. (1991). Stretching of the deep crust at the slow-spreading Southwest Indian Ridge. *Tectonophysics*, *190*(1). https://doi.org/10.1016/0040-1951(91)90355-v

Bachmann, F., Hielscher, R., & Schaeben, H. (2010). Texture analysis with MTEX - Free and open source software toolbox. *SSP*, *160*, 63–68. https://doi.org/10.4028/www.scientific.net/ssp.160.63

Bachmann, F., Hielscher, R., & Schaeben, H. (2011). Grain detection from 2d and 3d EBSD data-Specification of the MTEX algorithm. *Ultramicroscopy*, *111*(12), 1720–1733. https://doi.org/10.1016/j.ultramic.2011.08.002

Barsoum, M. W., Farber, L., & Introduction, I. (1999). *Dislocations, kink bands, and room-temperature plasticity*.

Basu, R. (1977). Textures, microstructures and deformation of ultramafic xenoliths from San Quintin, Baja California. *Tectonophysics*, *43*, 213–216.

Behn, M. D., & Ito, G. (2008). Magmatic and tectonic extension at mid-ocean ridges: 1. Controls on fault characteristics. *Geochemistry, Geophysics, Geosystems*, *9*(8). https://doi.org/10.1029/2008gc001965

Ben Ismail, W., Tommasi, A., Lopez-Sanchez, M. A., Rutter, E. W., & Barou, F. *Deformation of upper mantle rocks with contrasting initial fabrics in axial extension*. Retrieved from https://arxiv.org/abs/2101.03362

Bickert, M., Lavier, L., & Cannat, M. (2020). How do detachment faults form at ultraslow mid-ocean ridges in a thick axial lithosphere?. *Earth and Planetary Science Letters*, *533*. https://doi.org/10.1016/j.epsl.2019.116048

Borghini, G., Fumagalli, P., & Rampone, E. (2010). The stability of plagioclase in the upper mantle: Subsolidus experiments on fertile and depleted lherzolite. *Journal of Petrology*, *51*(1–2), 229–254. https://doi.org/10.1093/petrology/egp079

Boschi, C., Früh-Green, G. L., Delacour, A., Karson, J. A., & Kelley, D. S. (2006). Mass transfer and fluid flow during detachment faulting and development of an oceanic core complex, Atlantis Massif (MAR 30°N). *Geochemistry, Geophysics, Geosystems*, *7*(1). https://doi.org/10.1029/2005gc001074

Boudier, F., & Coleman, R. G. (1981). Cross section through the peridotite in the Samail Ophiolite, southeastern Oman Mountains. *Journal of Geophysical Research*https://doi.org/10.1029/JB086iB04p02573

Brunelli, D., Paganelli, E., & Seyler, M. (2014). Percolation of enriched melts during incremental open-system melting in the spinel field: A REE approach to abyssal peridotites from the Southwest Indian Ridge. *Geochimica et Cosmochimica Acta*. https://doi.org/10.1016/j.gca.2013.11.040

Buck, W. R., Lavier, L. L., & Poliakov, A. N. B. (2005). Modes of faulting at mid-ocean ridges. *Nature*, *434*(7034), 719–723. https://doi.org/10.1038/nature03358

Burnley, P. C., Cline, C. J., & Drue, A. (2013). Kinking in Mg_2GeO_4 olivine: An EBSD study. *American Mineralogist*, *98*(5–6), 927–931. https://doi.org/10.2138/am.2013.4224

Cann, J. R., Blackman, D. K., Smith, D. K., McAllister, E., Janssen, B., Mello, S., & Pascoe, A. R., (1997). Corrugated slip surfaces formed at ridge-transform intersections on the Mid-Atlantic Ridge. *Nature*, *385*(6614), 329–332. https://doi.org/10.1038/385329a0

Cannat, M. (1991). Plastic Deformation at an Oceanic Spreading Ridge: A Microstructural Study of Site 735 Gabbros (Southwest Indian Ocean). *Proceedings of the Ocean Drilling Program Scientific Results*, *118*, 399–408. https://doi.org/10.2973/odp.proc.sr.118.134.1991

Cannat, M. (1993). Emplacement of mantle rocks in the seafloor at mid-ocean ridges. *Journal of Geophysical Research*, *98*, 4163–4172. https://doi.org/10.1029/92jb02221

Cannat, M., Bideau, D., & Bougault, H. (1992). Serpentinized peridotites and gabbros in the Mid-Atlantic Ridge axial valley at 15°37′N and 16°52′N. *Earth and Planetary Science Letters*, *109*(1–2), 87–106. https://doi.org/10.1016/0012-821x(92)90076-8

Cannat, M., & Casey, J. F. (1995). An Ultramafic Lift at the Mid-Atlantic Ridge: Successive Stages of Magmatism in Serpentinized Peridotites from the 15°N Region. In *Mantle and Lower crust Exposed in Oceanic Ridges and in Ophiolites* (pp. 5–34). https://doi.org/10.1109/JSSC.2011.2118010

Cannat, M., Ceuleneer, G., & Fletcher, J. (1997). Localization of ductile strain and the magmatic evolution of gabbroic rocks drilled at the Mid-Atlantic Ridge (23°N). *Proceedings of the Ocean Drilling Program Scientific Results*, *153*. https://doi.org/10.2973/odp.proc.sr.153.006.1997

Cannat, M., Mevel, C., Maia, M., Deplus, C., Durand, C., Gente, et al. (1995). Thin crust, ultramafic exposures, and rugged faulting patterns at the Mid-Atlantic Ridge (22°-24°N). *Geology*, *23*(1), 49–52. https://doi.org/10.1130/0091-7613(1995)023<0049:tcuear>2.3.co;2

Cannat, M., Rommevaux-Jestin, C., Sauter, D., Deplus, C., & Mendel, V. (1999). Formation of the axial relief at the very slow spreading Southwest Indian Ridge (49° to 69°E). *Journal of Geophysical Research*, *104*(B10), 22825–22843. https://doi.org/10.1029/1999jb900195

Cannat, M., Sauter, D., Lavier, L., Bickert, M., Momoh, E., & Leroy, S. (2019). On spreading modes and magma supply at slow and ultraslow mid-ocean ridges. *Earth and Planetary Science Letters*, *519*, 223–233. https://doi.org/10.1016/j.epsl.2019.05.012

Cannat, M., Sauter, D., Mendel, V., Ruellan, E., Okino, K., Escartin, MV., et al. (2006). Modes of seafloor generation at a melt-poor ultraslow-spreading ridge. *Geology*, *34*(7), 605–608. https://doi.org/10.1130/g22486.1

Cannat, M., Sauter, D., & Rouméjon, S. (2012). Formation of an ultramafic seafloor at the Southwest Indian Ridge 62°-65°E : internal structure of detachment faults and sparse volcanism documented by sidescan sonar and dredges. *AGU Fall Meeting Abstracts*.

Carlut, V., & Schmid, F. (2016). Mid-ocean-ridge seismicity reveals extreme types of ocean lithosphere. *Nature*, *535*(7611), 276–279. https://doi.org/10.1038/nature18277

Carter, N. L., & Ave'lallemant, H. G. (1970). High temperature flow of dunite and peridotite. *Geological Society of America Bulletin*, *81*, 2181–2202. https://doi.org/10.1130/0016-7606(1970)81[2181:htfoda]2.0.co;2

Ceuleneer, G., & Cannat, M. (1997). 2. High-Temperature Ductile Deformation of Site 920 Peridotites. *Proceedings of the Ocean Drilling Program. Scientific Results*, *153*(June), 23–34. https://doi.org/10.2973/odp.proc.sr.153.002.1997

Chatzaras, V., Tikoff, B., Kruckenberg, S. C., Titus, S. J., Teyssier, C., & Drury, M. R. (2020). Stress variations in space and time within the mantle section of an oceanic transform zone: Evidence for the seismic cycle. *Geology*, *48*(6), 569–573. https://doi.org/10.1130/G47137.1

Chen, J., Crawford, W. C., & Cannat, M. (2020). Microseismicity constraints on brittle lithosphere thickness at a nearly amagmatic spreading corridor of the ultraslow Southwest Indian Ridge. In: AGU Fall Meeting Abstracts.

Combier, Mathilde, Sauter, D., Escartín, J., Lavier, L., & Picazo, S. (2009). Oceanic corrugated surfaces and the strength of the axial lithosphere at slow spreading ridges. *Earth and Planetary Science Letters*. https://doi.org/10.1016/j.epsl.2009.09.020

Cross, A. J., Hirth, G., & Prior, D. J. (2017). Effects of secondary phases on crystallographic preferred orientations in mylonites. *Geology*, *45*(10), 955–958. https://doi.org/10.1130/g38936.1

deMartin, B. J., Pablo Canales, J., Humphris, S. E., & Humphris, S. E. (2007). Kinematics and geometry of active detachment faulting beneath the Trans-Atlantic geotraverse (TAG) hydrothermal field on the Mid-Atlantic Ridge. *Geology*, *35*(8), 711–714. https://doi.org/10.1130/g23718a.1

Demouchy, S., Tommasi, A., Boffa Ballaran, T., & Cordier, P. (2013). Low strength of Earth's uppermost mantle inferred from tri-axial deformation experiments on dry olivine crystals. *Physics of the Earth and Planetary Interiors*, *220*, 37–49. https://doi.org/10.1016/j.pepi.2013.04.008

Dick, H. J. B., Lin, J., & Schouten, H. (2003). An ultraslow-spreading class of ocean ridge. *Nature*. https://doi.org/10.1038/nature02128

Dick, H. J. B., Lissenberg, C. J., & Warren, J. M. (2010). Mantle Melting, Melt Transport, and Delivery Beneath a Slow-Spreading Ridge: The Paleo-MAR from 23 15′N to 23 45′N. *Journal of Petrology*, *51*(1–2), 425–467. https://doi.org/10.1093/petrology/egp088

Dick, H. J. B., Ozawa, K., Meyer, P. S., Niu, Y., Robinson, P. T., Constantin, M. et al. (2002). Primary silicate mineral chemistry of a 1.5-km section of very slow spreading lower ocean crust: ODP Hole 735B, Southwest Indian Ridge. *Proceedings of the Ocean Drilling Program. 176*. https://doi.org/10.2973/odp.proc.sr.176.001.2002

Duarte, V. J. F., Kaczmarek, M.-A., Vonlanthen, P., Putlitz, B., & Müntener, O. (2020). Hydration of a mantle shear zone beyond serpentine stability: A possible link to microseismicity along ultraslow spreading ridges? Journal of Geophysical Research. *Solid Earth*, *125*, e2020JB019509. https://doi.org/10.1029/2020JB019509

Durham, W. B., & Goetze, C. (1977). A comparison of the creep properties of pure forsterite and iron-bearing olivine. *Tectonophysics*, *40*(3–4). https://doi.org/10.1016/0040-1951(77)90063-4

Ellis, S., & Stockhert, B. (2004). Elevated stresses and creep rates beneath the brittle–ductile transition caused by seismic faulting in the upper crust. *Journal of Geophysical Research 109*, B05407. http://dx.doi.org/10.1029/2003jb002744

Escartín, J., Andreani, M., Hirth, G., & Evans, B. (2008). Relationships between the microstructural evolution and the rheology of talc at elevated pressures and temperatures. *Earth and Planetary Science Letters*, *268*(3–4), 463–475. https://doi.org/10.1016/j.epsl.2008.02.004

Escartín, J., Hirth, G., & Evans, B. W. (1997). Implications for Mohr-Coulomb theory and the strength of faults. *Journal of Geophysical Research*, *102*(96), 2897–2913. https://doi.org/10.1029/96jb02792

Frets, E. C., Tommasi, A., Garrido, C. J., Vauchez, A., Mainprice, D., Targuisti, K., & Amri, I. (2014). The Beni Bousera Peridotite (Rif Belt, Morocco): An oblique-slip low-angle shear zone thinning the subcontinental mantle lithosphere. *Journal of Petrology*, *55*, 283–313. https://doi.org/10.1093/petrology/egt067

Garcés, M., & Gee, J. S. (2007). Paleomagnetic evidence of large footwall rotations associated with low-angle faults at the Mid-Atlantic Ridge. *Geology*, *35*, 279–282. https://doi.org/10.1130/g23165a.1

Gouriet, K., Cordier, P., Garel, F., Thoraval, C., Demouchy, S., Tommasi, A., & Carrez, P. (2019). Dislocation dynamics modeling of the power-law breakdown in olivine single crystals: Toward a unified creep law for the upper mantle. *Earth and Planetary Science Letters*, *506*(January), 282–291. https://doi.org/10.1016/j.epsl.2018.10.049

Grevemeyer, I., Hayman, N. W., Lange, D., Peirce, C., Papenberg, C., Van Avendonk, et al. (2019). Constraining the maximum depth of brittle deformation at slow- and ultraslow-spreading ridges using microseismicity. *Geology*, *47*(11), 1069–1073. https://doi.org/10.1130/g46577.1

Hansen, L. N., Cheadle, M. J., John, B. E., Swapp, S. M., Dick, H. J. B., Tucholke, B. E., & Tivey, M. A. (2013). Mylonitic deformation at the Kane oceanic core complex: Implications for the rheological behavior of oceanic detachment faults. *Geochemistry, Geophysics, Geosystems*, *14*(8), 3085–3108. https://doi.org/10.1002/ggge.20184

Harigane, Y., Abe, N., Michibayashi, K., Kimura, J.-I., & Chang, Q. (2016). Melt-rock interactions and fabric development of peridotites from North Pond in the Kane area, Mid-Atlantic Ridge: Implications of microstructural and petrological analyses of peridotite samples from IODP Hole U1382A. *Geochemistry, Geophysics, Geosystems*, *17*, 2298–2322. https://doi.org/10.1002/2016gc006429

Herwegh, M., Linckens, J., Ebert, A., Berger, A., & Brodhag, S. H. (2011). The role of second phases for controlling microstructural evolution in polymineralic rocks: A review. *Journal of Structural Geology*, *33*(12), 1728–1750. https://doi.org/10.1016/j.jsg.2011.08.011

Hidas, K., Tommasi, A., Garrido, C. J., Padrón-Navarta, J. A., Mainprice, D., Vauchez, A., et al. (2016). Fluid-assisted strain localization in the shallow subcontinental lithospheric mantle. *Lithos*, *262*, 636–650. https://doi.org/10.1016/j.lithos.2016.07.038

Hirth, G., & Kohlstedt, D. (2003). Rheology of the Upper Mantle and the Mantle Wedge: A View from the Experimentalists. *Inside the Subduction Factory*, 83–105. https://doi.org/10.1029/138gm06

Ildefonse, B., Blackman, D. K., John, B. E., Ohara, Y., Miller, D. J., & MacLeod, C. J. (2007). Oceanic core complexes and crustal accretion at slow-spreading ridges. *Geology*, *35*, 623. https://doi.org/10.1130/g23531a.1

Jammes, S., Lavier, L. L., & Reber, J. E. (2015). Localization and delocalization of deformation in a bimineralic material. *Journal of Geophysical Research: Solid Earth*, *120*(5), 3649–3663. https://doi.org/10.1002/2015jb011890

Jaroslow, G. E., Hirth, G., & Dick, H. J. B. (1996). Abyssal peridotite mylonites: Implications for grain-size sensitive flow and strain localization in the oceanic lithosphere. *Tectonophysics*, *256*, 17–37. https://doi.org/10.1016/0040-1951(95)00163-8

Kaczmarek, M. A., & Tommasi, A. (2011). Anatomy of an extensional shear zone in the mantle, Lanzo massif. Italy. *Geochemistry, Geophysics, Geosystems*, *12*, 2011GC003627 https://doi.org/10.1029/2011gc003627

Karato, S.-I., Paterson, M. S., & Fitzgerald, J. D. (1986). Rheology of synthetic olivine aggregates: Influence of grain size and water. *Journal of Geophysical Research*, *91*(B8), 8151–8176. https://doi.org/10.1029/jb091ib08p08151

Kohli, A. H., & Warren, J. M. (2020). Evidence for a deep hydrologic cycle on oceanic transform faults. *Journal of Geophysical Research: Solid Earth*, *125*, e2019JB017751. https://doi.org/10.1029/2019jb017751

Lavier, L. L., & Buck, R. W. (2002). Half graben versus large-offset low-angle normal fault: Importance of keeping cool during normal faulting. *Journal of Geophysical Research*, *107(B6)*, 2122. https://doi.org/10.1029/2001JB000513

Le Roux, V., Tommasi, A., & Vauchez, A. (2008). Feedback between melt percolation and deformation in an exhumed lithosphere-asthenosphere boundary. *Earth and Planetary Science Letters*, *274*(3–4), 401–413. https://doi.org/10.1016/j.epsl.2008.07.053

Lilly, C. J., Searle, R. C., Murton, B. J., Casey, J. F., Mallows, C., Unsworth, et al. (2009). Life cycle of oceanic core complexes. *Earth and Planetary Science Letters*, *287*(3–4), 333–344. https://doi.org/10.1016/j.epsl.2009.08.016

Linckens, J., Herwegh, M., & Müntener, O. (2015). Small quantity but large effect - How minor phases control strain localization in upper mantle shear zones. *Tectonophysics*, *643*, 26–43. https://doi.org/10.1016/j.tecto.2014.12.008

Linckens, J., Herwegh, M., Mntener, O., & Mercolli, I. (2011). Evolution of a polymineralic mantle shear zone and the role of second phases in the localization of deformation. *Journal of Geophysical Research*, *116*(6), 1–21. https://doi.org/10.1029/2010jb008119

MacLeod, C. J., Escartín, J., Banerji, D., Banks, G. J., Gleeson, M., Irving, et al, . (2002). Direct geological evidence for oceanic detachment faulting: The Mid-Atlantic Ridge, 15°45′N. *Geology*, *30*(10), 879–882. https://doi.org/10.1130/0091-7613(2002)030<0879:dgefod>2.0.co;2

Matysiak, A. K., & Trepmann, C. A. (2015). The deformation record of olivine in mylonitic peridotites from the Finero Complex, Ivrea Zone: Separate deformation cycles during exhumation. *Tectonics*, *34*(12), 2514–2533. https://doi.org/10.1002/2015tc003904

Minshull, T. A., Muller, M. R., & White, R. S. (2006). Crustal structure of the Southwest Indian Ridge at 66°E: seismic constraints. *Geophysical Journal International*, *166*(1), 135–147. https://doi.org/10.1111/j.1365-246x.2006.03001.x

Morris, A., Gee, J. S., Pressling, N., John, B. E., MacLeod, C. J., Grimes, C. B., & Searle, R. C. (2009). Footwall rotation in an oceanic core complex quantified using reoriented Integrated Ocean Drilling Program core samples. *Earth and Planetary Science Letters*, *287*, 217–228. https://doi.org/10.1016/j.epsl.2009.08.007

Newman, J., Lamb, W. M., Drury, M. R., & Vissers, R. L. M. (1999). Deformation processes in a peridotite shear zone: reaction-softening by an H_2O-deficient, continuous net transfer reaction. *Tectonophysics*, *303*(1–4), 193–222. https://doi.org/10.1016/S0040-1951(98)00259-5

Olive, J.-A., Behn, M. D., & Tucholke, B. E. (2010). The structure of oceanic core complexes controlled by the depth distribution of magma emplacement. *Nature Geoscience*, *3*(7), 491–495. https://doi.org/10.1038/ngeo888

Paquet, M., Cannat, M., Brunelli, D., Hamelin, C., & Humler, E. (2016). Effect of melt/mantle interactions on MORB chemistry at the easternmost Southwest Indian Ridge (61°–67°E). *Geochemistry, Geophysics, Geosystems*, *17*, 4605–4640. https://doi.org/10.1002/2016gc006385

Parnell-Turner, R., Escartín, J., Olive, J.-A., Smith, D. K., & Petersen, S. (2018). Genesis of corrugated fault surfaces by strain localization recorded at oceanic detachments. *Earth and Planetary Science Letters*, *498*, 116–128. https://doi.org/10.1016/j.epsl.2018.06.034

Picazo, S., Cannat, M., Delacour, A., Escartín, J., Rouméjon, S., & Silantyev, S. (2012). Deformation associated with the denudation of mantle-derived rocks at the Mid-Atlantic Ridge 13°–15°N: The role of magmatic injections and hydrothermal alteration. *Geochemistry, Geophysics, Geosystems*, *13*(4), 1–30. https://doi.org/10.1029/2012gc004121

Precigout, J., Gueydan, F., Gapais, D., Garrido, C. J., & Essaifi, A. (2007). Strain localization in the subcontinental mantle - a ductile alternative to the brittle mantle. *Tectonophysics*, *445*(3–4), 318–336. https://doi.org/10.1016/j.tecto.2007.09.002

Prigent, C., Warren, J. M., Kohli, A. H., & Teyssier, C. (2020). Fracture-mediated deep seawater flow and mantle hydration on oceanic transform faults. *Earth and Planetary Science Letters*, *532*, 115988. https://doi.org/10.1016/j.epsl.2019.115988

Raleigh, C. B. (1968). Mechanisms of plastic deformation of olivine. *Journal of Geophysical Research*, *73*(16), 5391–5406. https://doi.org/10.1029/jb073i016p05391

Reston, T. (2018). Flipping detachments: The kinematics of ultraslow spreading ridges. *Earth and Planetary Science Letters*, *503*, 144–157. https://doi.org/10.1016/j.epsl.2018.09.032

Ross, J. V., & Nielsen, K. C. (1978). High-temperature flow of wet polycrystalline enstatite. *Tectonophysics*, *44*(1–4). https://doi.org/10.1016/0040-1951(78)90072-0

Roumejon, S., Cannat, M., Agrinier, P., Godard, M., & Andreani, M. (2015). Serpentinization and Fluid Pathways in Tectonically Exhumed Peridotites from the Southwest Indian Ridge (62–65 E). *Journal of Petrology*, *56*(4), 703–734. https://doi.org/10.1093/petrology/egv014

Sauter, D., Cannat, M., Rouméjon, S., Andreani, M., Birot, D., Bronner, A., et al. (2013). Continuous exhumation of mantle-derived rocks at the Southwest Indian Ridge for 11 million years. *Nature Geoscience*, *6*(4), 314–320. https://doi.org/10.1038/ngeo1771

Schmid, C. B., John, B. E., Cheadle, M. J., & Wooden, J. L. (2008). Protracted construction of gabbroic crust at a slow spreading ridge: Constraints from 206Pb/238U zircon ages from Atlantis Massif and IODP Hole U1309D (30°N, MAR). *Geochemistry, Geophysics, Geosystems*, *9*(8). https://doi.org/10.1029/2008gc002063

Schroeder, T., & John, B. E. (2004). Strain localization on an oceanic detachment fault system, Atlantis Massif, 30°N, Mid-Atlantic Ridge. *Geochemistry, Geophysics, Geosystems*, *5*. https://doi.org/10.1029/2004GC000728

Seyler, M., Cannat, M., & Mével, C. (2003). Evidence for major-element heterogeneity in the mantle source of abyssal peridotites from the Southwest Indian Ridge (52° to 68°E). *Geochemistry, Geophysics, Geosystems*, *4*(2), 1525–2027. https://doi.org/10.1029/2002gc000305

Seyler, M., Lorand, J.-P., Dick, H. J. B., & Drouin, M. (2007). Pervasive melt percolation reactions in ultra-depleted refractory harzburgites at the Mid-Atlantic Ridge, 15° 20′N: ODP Hole 1274A. *Contributions to Mineralogy and Petrology*, *153*(3), 303–319. https://doi.org/10.1007/s00410-006-0148-6

Seyler, M., Lorand, J.-P., Toplis, M. J., & Godard, G. (2004). Asthenospheric metasomatism beneath the mid-ocean ridge: Evidence from depleted abyssal peridotites. *Geology*, *32*(4), 301–304. https://doi.org/10.1130/g20191.1

Smith, D. K., Cann, J. R., & Escartín, J. (2006). Widespread active detachment faulting and core complex formation near 13° N on the Mid-Atlantic Ridge. *Nature*, *442*(7101), 440–443. https://doi.org/10.1038/nature04950

Tucholke, B. E., Behn, M. D., Buck, W. R., & Lin, J. (2008). Role of melt supply in oceanic detachment faulting and formation of megamullions. *Geology*, *36*(6), 455–458. https://doi.org/10.1130/g24639a.1

Van der Wal, D., Chopra, P., Drury, M., & Gerald, J. F. (1993). Relationships between dynamically recrystallized grain size and deformation conditions in experimentally deformed olivine rocks. *Geophysical Research Letters*, *20*(14), 1479–1482. https://doi.org/10.1029/93gl01382

Warren, J. M., & Hirth, G. (2006). Grain size sensitive deformation mechanisms in naturally deformed peridotites. *Earth and Planetary Science Letters*, *248*(1–2), 423–435. https://doi.org/10.1016/j.epsl.2006.06.006

Yu, Z., Li, J., Niu, X., Rawlinson, N., Ruan, A., Wang, et al. (2018). Lithospheric structure and tectonic processes constrained by microearthquake activity at the central ultraslow-spreading Southwest Indian Ridge (49.2° to 50.8°E). *Journal of Geophysical Research: Solid Earth*, *123*(8), 6247–6262. https://doi.org/10.1029/2017JB015367